Unraveling weathering episodes in Tertiary regoliths by kaolinite dating (Western Ghats, India)

Maximilien Mathian, Julie Aufort, Jean-Jacques Braun, Jean Riotte,
Madeleine Sélo, Etienne Balan, Emmanuel Fritsch, Shrema Bhattacharya,
Thierry Allard

Unraveling weathering episodes in Tertiary regoliths by kaolinite dating (Western Ghats, India)

Maximilien Mathian [a,*], Julie Aufort [a], Jean-Jacques Braun [b], Jean Riotte [b], Madeleine Selo [a], Etienne Balan [a], Emmanuel Fritsch [a], Shrema Bhattacharya [c], Thierry Allard [a]

[a] *Sorbonne Université, Institut de Minéralogie, de Physique des Matériaux et de Cosmochimie, UMR CNRS 7590, IRD, MNHN, 4 Place Jussieu, 75005, France*
[b] *Géosciences Environnement Toulouse, Observatoire Midi-Pyrénées, 14 avenue E.Belin, 31400 Toulouse, France*
[c] *Physical Research Laboratory, Geoscience Division, Ahmedabad 380009, India*

ABSTRACT

Secondary minerals in soils can record climatic changes affecting continental surfaces over geological times. Their dating should refine our present knowledge about their potential periods of formation as well as their relations with the ongoing change of climate and erosion/weathering regimes. In the present study, twenty kaolinite samples from two lateritic profiles of the Karnataka plateau, an intensively studied area in the southern India, have been dated using electron paramagnetic resonance (EPR) spectroscopy. Kaolinite ages vary between $0.229_{\pm 0.24}$ Ma to $40.73_{\pm 15.37}$ Ma. Four different groups of age can be identified with ages clustered around 1.0, 3.5, 9.0 and 39.0 Ma. These groups of age indicate local preferential weathering periods that coincide with distinct Indian climatic events described in independent studies, such as monsoon strengthening. Thus, regional or subcontinental factors likely prevailed over global forcing in the imprint of climatic events in the regolith profiles. These results confirm that despite their simple mineralogy, laterites can contain several relictual and coexisting generations of secondary minerals and that EPR dating of kaolinite contributes to unraveling the complex history of continental surfaces over geological periods.

1. Introduction

The regolith, composed of saprolite and soil *stricto sensu* horizons, is an important part of the Critical Zone (CZ), i.e. the thin fragile zone at the Earth's surface that supports life (Brantley et al., 2007). It results from the complex interactions between minerals, life and water which largely depend on the interplay of climatic and tectonic parameters at a global scale (e.g. West et al., 2005; Dixon and Von Blanckenburg, 2012, Guillocheau et al., 2018). Over the geological times, the regolith can record various climatic influences prevailing during the formation of secondary minerals (Girard et al., 2000, 2002; Vasconcelos et al., 2015; Yapp, 2000). Nevertheless, topography, primary rock composition and biological factors also influence the development of weathering profiles. In addition, the dating of old regolith components, composed of multiple generations of poorly ordered and finely divided authigenic minerals, remains a challenging task because of the difficulty to physically isolate the different generations of minerals (e.g. Vasconcelos, 1999; Girard et al., 2000, 2002; Balan et al., 2005; Bonnet et al., 2016).

Thick lateritic covers have developed in the intertropical zone and are present on more than 30% of the continental surfaces. Due to their important thickness, laterites account for about 80% of the global Earth regolith volume (Tardy and Roquin, 1998; Nahon, 1991, 2003). Their mineralogy is dominated by authigenic kaolinite and Fe/Al oxide/oxyhydroxide (Nahon, 1991). These minerals represent archives of paleoclimates related to specific weathering events (Retallack, 2010). In many cases, a vertical distribution of several generations of secondary minerals is observed in the same profile (e.g. Bird et al., 1993; Muller et al., 1995; Girard et al., 2000, 2002; Balan et al., 2005, 2007; Fritsch et al., 2011). Absolute dating of laterites from previous studies revealed that they have Mesozoic and Cenozoic ages in India, Africa or South America (Vasconcelos et al., 1994, 2015; Balan et al., 2005; Bonnet et al., 2016; Allard et al., 2018). In case of the Amazon basin, absolute age records were consistent with those obtained from weathering mass balance calculations (about ten million years old, Lucas, 1989). Ages of laterites were also discussed using the results of mass balance calculation results on different soil locations in India (Braun et al., 2009).

In the research of paleoclimatic signatures, laterites from the Indian sub-continent deserve a special attention because of the substantial drift of the Indian platform, from a latitude of 60°S during the Trias (India was a part of the Pangea) to its current position (northern point around 30°N) reached ca 30 Ma ago (Chatterjee et al., 2013). During

this 137 Ma long drift, the Indian plate moved through different climatic zones. Although the onset of Indian laterites formation is debated, it is likely older than the Mid-Cretaceous (Kumar, 1986; Tardy et al., 1991, Tardy and Roquin, 1998; Chatterjee et al., 2013). Dating of manganese-rich laterites upon Dharwar Plateau indicates major weathering periods at 53–50 Ma and 37–23 Ma in the highlands, where the former reflecting impact of the Eocene climatic optimum when India was located in the equatorial belt and the latter reflecting the weathering response to late Oligocene warming, respectively (Bonnet et al., 2014, 2016).

This study focuses on two lateritic profiles from the Indian subcontinent, located in the South of the Karnataka plateau near the localities of Mananthavady and Payoddu in the humid zone of a sharp longitudinal climatic gradient (Gunnell and Bourgeon, 1997). The objectives are to identify co-existing generations of kaolinite, as a major secondary mineral of non-indurated laterites, to analyze their spatial distribution in the weathering profile and to examine their link to the past local or global climate events using dating by the electron paramagnetic resonance (EPR) spectroscopy. This dating methodology, here applied for the first time to an Indian soil, is based on the analysis of the paramagnetic defects of the kaolinite structure that are induced by natural exposure to ionizing radiations (Ikeya, 1993; Clozel et al., 1994; Balan et al., 2005).

2. Geological context

The Western Ghats Escarpment (WGE) is a 1500 km long passive continental margin parallel to the coast of the Arabian Sea. This escarpment resulted from two continental breakups: 1) between India and Madagascar (ca 90 Ma); 2) between India and Seychelles (ca 71–62 Ma) (Collier et al., 2008; Chatterjee et al., 2013; Ramkumar et al., 2016). Its denudation and retreat had begun early Tertiary (see Beauvais et al., 2016). Its current geomorphology can be attributed to several factors such as denudational/erosional uplift (Widdowson, 1997; Gunnell and Fleitout, 1998) or tectonically driven uplift (Kale and Shejwalkar, 2008). The resulting regional organization (Fig. 1A) from West to East is characterized by the presence of: 1) the flat western coastal plains with maximum elevation of ~500 m, 2) the Ghats escarpment, with an elevation varying from 600 to 2200 m at a distance of maximum up to 70 km of the coast, 3) the elevated inland plateau succession (Gunnell et al., 2003). Based on thermochronological data, several authors described a steady state erosion rate between the lowlands and uplands of this chain since 40 Ma (Gunnell et al., 2003; Mandal et al., 2015) that could be linked to an erosion/uplift equilibrium. Based on duricrust dating, other explained that low erosion rates characterizing slow denudation regimes can be reached shortly after the continental breakup that formed the WGE (Beauvais et al., 2016).
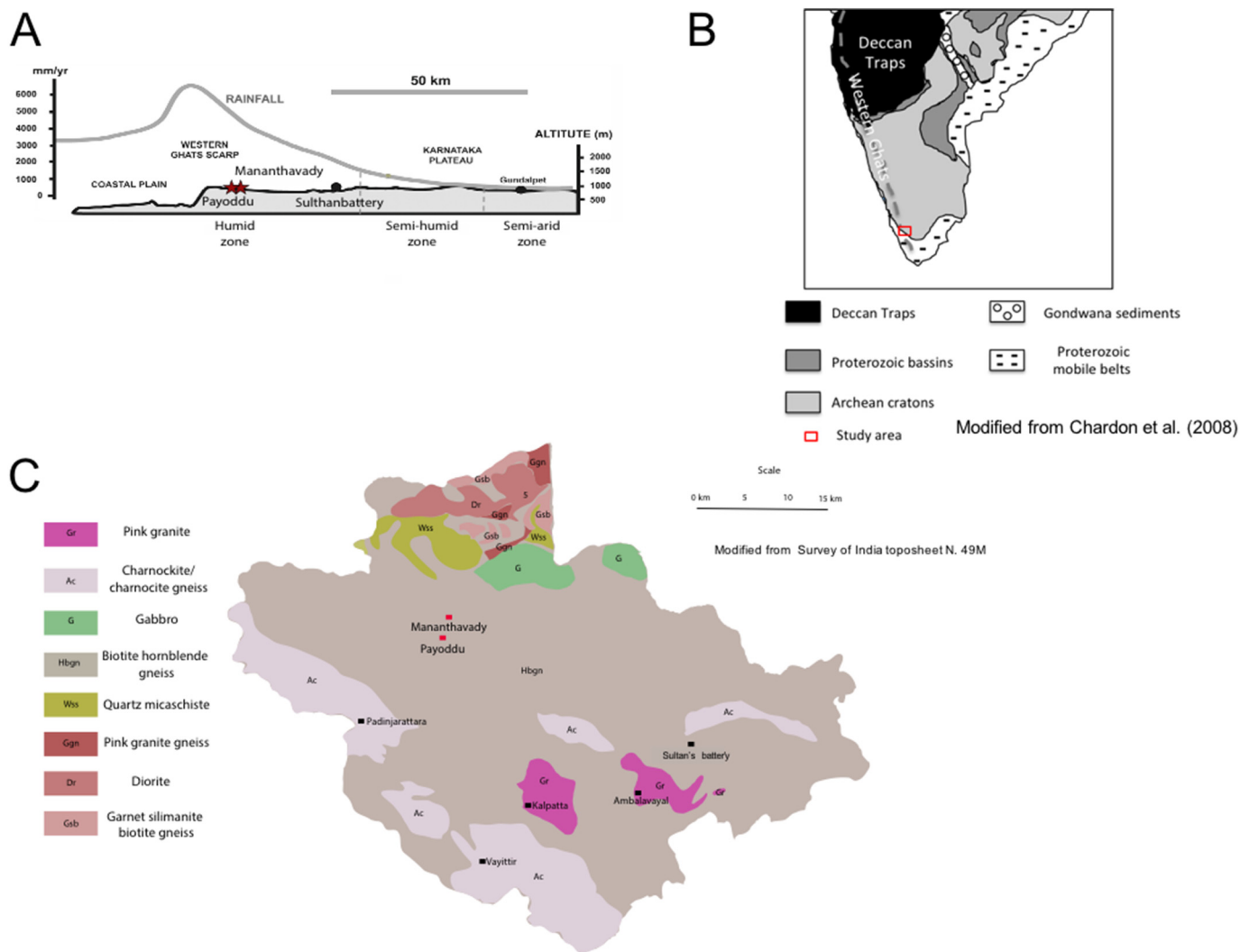
Fig. 1. Geology and geomorphology of the Karnataka plateau, with, A: The topography and associated rainfall (modified from Violette et al. (2010)) of a Western Ghats cross-section from the sea to the eastern edge of the Karnataka plateau. B: Simplified schematic diagram showing the main Indian/stratigraphic divisions (derived from Chardon et al., 2008) along with the studied area. C: simplified regional geological map (modified from the Survey of India toposheet N. 49 M (1995) and 58A (1970)).

These data could be linked to an erosion/uplift equilibrium. From North to South, Western India is divided into two geological regions (Fig. 1B), the northern Deccan Traps, mainly covered by flood basalts, and the southern Archean Dharwar craton, with a bedrock mainly composed by charnockite, Archean greenstones and Archean gneiss rich in biotite and hornblende (Chardon et al., 2008).

Several WGE weathering surface ages have been proposed from paleomagnetic investigations (Schmidt et al., 1983; Kumar, 1986) and some lateritic duricrusts and bauxites have already been dated along this scarp using the $^{40}Ar/^{39}Ar$ dating methodology (Bonnet et al., 2014, 2016). These methodologies have constrained the formation of these surfaces from the end of the Cretaceous to the Pliocene. Several intense weathering periods have been identified using $^{40}Ar/^{39}Ar$ dating: 1) a global lateritic weathering event between 53 and 45 Ma, affected all the scarp regions including a large part of India, 2) a 37 to 23 Ma weathering event was responsible for the duricrusts and bauxites formation in the plateau along the scarp, 3) a 24 to 19 Ma period was detected for coastal laterites formation (i.e. secondary laterites) and 4) more recent short events were only detected in some coastal plain laterites.

The Western Ghats Escarpment directly lies across the path of the southwest Indian monsoon (Gunnell, 1997). Acting as an orographic natural barrier, this margin is the cause of an important west-east precipitation gradient (Fig. 1A) with a sharp eastward decrease of rainfall (Braun et al., 2009; Violette et al., 2010; Ramkumar et al., 2016). Precipitation are above 3000 mm per year in the coastal plain, rising to more than 6000 mm per year in the scarp region and falling to 900 mm per year in the eastern semi-arid zone of the Karnataka plateau (South India). This gradient is also correlated to a geomorphologic gradient (Gunnell and Bourgeon, 1997). The western part of the plateau is characterized by a multi-convex landform while the eastern part, in the semi-arid region, exhibits a multi-concave landform. The erosion of ferralsols (referred to as laterites in this paper) developed in this region also increases from west to east. Almost complete lateritic profiles (from saprolite to topsoil) can be found near to the scarp, whereas only truncated saprolites occur in the eastern part of this plateau.

The present study focuses on partially eroded laterite profiles of the Kabini river basin, in the humid zone of the Karnataka plateau, where precipitation ranges from 3000 to 4000 mm per year. South-west monsoon represents more than 75% of the annual precipitation (Ramkumar et al., 2016). This monsoon regime depends on the relief-controlled troposphere structure and particularly on the Tibetan highlands affecting the atmospheric circulation (e.g. Gunnell, 1997 and ref. therein). The average local temperature is around 24 °C. In this part of the plateau the ^{10}Be derived erosion rate is around 20 m·Ma^{-1} (Mandal et al., 2015). One profile, referred to as Mananthavady profile, is accessible within an open pit located at a hill slope close to the locality of Mananthavady (11.80N-76.00E). The second profile, referred to as the Payoddu profile, is located close to the same locality but at the base of another hillslope. Both soils developed on the same biotite and hornblende rich gneiss (Fig. 1C).

3. Samples

Sixteen samples were selected from the laterite profile of Mananthavady (Fig. 2A) and four samples were selected from the less complex laterite profile of Payyodu (Fig. 2B). Both profiles are described in detail in the Supplementary File 1. Field observations indicate that these weathering profiles are eroded ferralsols. Their complex organization (strong heterogeneities in mineralogy/texture/structure, folded horizons, horizon pouches) derives from the foliation of the parent gneiss with nearly vertical dip (Fig. 2A and B). The weathered zones of both profiles are more than 20 m thick and only their upper parts were sampled. Despite of their complexity, the selected profiles display the succession of saprolite, mottled zone and topsoil from bottom to top, respectively.

To obtain petrographic and fission tracks data from each main soil horizon, nine and four thin sections were prepared from Mananthavady and Payoddu profiles, respectively.

4. Methodology

Samples were dried at room temperature and sieved. The mineralogical composition of fraction size lower than 2 mm was determined by XRD measurements using a Panalytical Pro MPD equipped with a X'Celerator detector and Co-Kα radiations. Analyses were performed for a 2θ range of 3 to 65°, with steps of 0.017° and an acquisition of 480 ms per step.

The chemical composition was determined at the Service d'Analyse des Roches et Minéraux (SARM, Nancy, France) by inductively coupled plasma atomic optical emission spectrometry (ICP-OES) for major elements quantification and inductively coupled plasma atomic mass spectrometry (ICPMS) for the trace elements quantification. See http://www.crpg.cnrs-nancy.fr/SARM/index.html for further information including the experimental errors. Based on the chemical analyses, mass balances have been estimated (Oh and Richter, 2005; Braun et al., 2012).

Kaolinite samples were purified by a selective dissolution of iron oxides and oxyhydroxides using several dithionite-citrate-bicarbonate treatments (Mehra and Jackson, 1960) and subsequent sorting of the clay size fraction (<2 μm) by sedimentation. These purified clay size fraction samples will be further referred to as 'purified samples'.

Fourier transform infrared (FTIR) spectroscopic measurements were performed using a Nicolet Magna 560 FTIR spectrometer with purged dry air. All samples were analyzed in the transmission mode, using KBr pellets made of 1 mg of purified sample mixed with 150 mg of KBr and dried in an oven during 24 h at 190 °C. Spectra were recorded at room temperature by averaging 100 spectra with a resolution of 2 cm^{-1} in the 400–4000 cm^{-1} range.

^{235}U induced fission tracks mapping was performed on five polished thin sections of structurally-preserved soil samples embedded in resin, using an external detector (Kapton®) as described by Price and Walker (1963) and Kleeman and Lovering (1967). The thin sections were covered with a Kapton® foil and jointly irradiated, using thermal neutrons, with standard glasses (i.e. SRM-613 from the National Bureau of Standard, Washington) for the calibration of the U content (12.33 μg·g^{-1} of normalized U for the SRM-613). Irradiations were performed at the FRM2 reactor in Munich (Germany) during 600 s using an instant flux of $1.15 \cdot 10^{13}$ n·cm^{-2}·s^{-1}. Fission tracks registered in the Kapton® foils were revealed and then counted using an optical microscope with an objective of 10×100 magnification in transmitted light. The revelation of the fission tracks induced in the Kapton® foils was performed by an etching of 8 min in an aqueous solution of 14% NaClO and 12% NaCl heated at 100 °C (Selo, 1983).

The EPR spectra were recorded at X-Band (9.44 GHz) using a Bruker EMXplus™ spectrometer equipped with a high sensibility cavity. Acquisition was operated with a microwave power of 40 mW and a magnetic field modulation with frequency of 100 kHz and amplitudes of 0.3 mT (Radiation Induced Defects (RID) spectra) or 0.5 mT (total spectra). Full spectra were measured at room temperature for the assessment of kaolinite crystalline order and RID concentration measurements were performed at 110 K. The EPR signals are characterized by effective g values defined by the resonance condition:

$$h\nu = g\beta H \qquad (1)$$

where h is the Planck constant, ν is the microwave frequency, ß is the Bohr magneton and H the magnetic field. The DPPH standard (g = 2.0036) was used to calibrate the g values.

The RID concentration was assessed from the amplitude of the perpendicular component of the RID signal (dominantly due to the so-called "A-center"). In order to compare the EPR amplitudes, calibrated
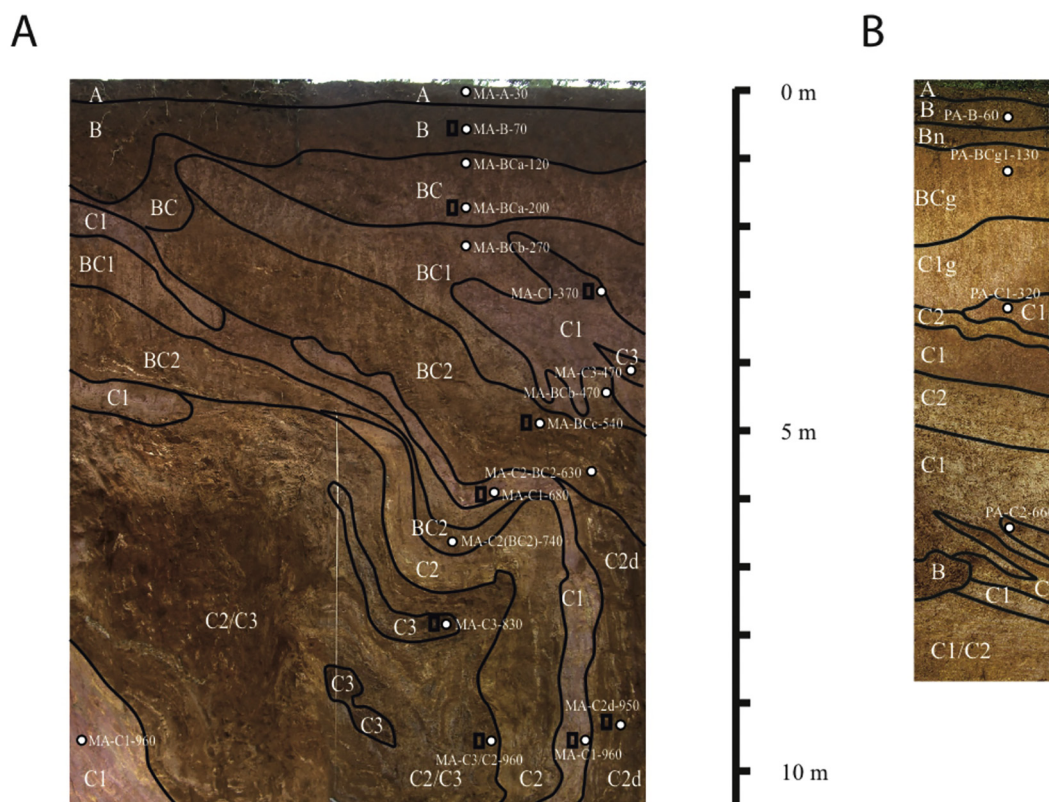
Fig. 2. A: Mananthavady regolith profile showing a 10 m thick laterite organized in 10 types of horizons (see the geological context and Supplementary File 1 for further description). The complex organization of this profile is inherited from the parent rock organization: a highly heterogeneous gneiss. A set of 16 samples has been selected along this profile for the dating analyses. B: Payoddu regolith profile showing a 9 m thick laterite organized in 8 horizons (see the geological context for further descriptions). Its organization is also complex. A set of 4 samples has been selected along this profile for the dating analyses.

silica tubes (suprasyl grade) were filled with a constant volume of sample and carefully placed at the same position in the cavity. The spectra were normalized using the sample weight and recording gain as described in Balan et al. (2005). The standard error on measured RID normalized amplitude was equal to 15%.

Artificial irradiations used for dosimetry were performed on the ARAMIS electrostatic accelerator (Orsay, France). A beam of 1.5 MeV He^+ ions with a 0.3 A current has been used to simulate radiation effects due to alpha particles. For each measurement, 35 mg of purified sample was deposited by sedimentation on a circular steel plate to obtain a layer with a constant thickness of 4 μm, which is the penetration depth of 1.5 MeV He^+ ions in kaolinite as calculated by the SRIM code (Ziegler et al., 2010). Six different ion fluences were used (3×10^{11}, 6×10^{11}, 10^{12}, 3×10^{12}, 6×10^{12} and 10^{13} ions·cm^{-2}) to produce 6 irradiation doses from 70 to 2342 kGy.

5. Results

5.1. Characterization of the lateritic profiles

5.1.1. Mineralogy and petrography of the laterite profiles

Despite heterogeneity of both profiles (Table 1 and Supplementary File 2), the sample mineralogy is dominantly composed of quartz, kaolinite and goethite. The Payoddu samples are richer in kaolinite than the Mananthavady ones. Minor phases such as chlorite, anatase, gibbsite or hematite can also be observed. Gibbsite is only detectable in the soil horizons (i.e. A and B) of the Mananthavady profile. The occurrence and proportion of the other mineral phases cannot be easily linked with any vertical gradient and more likely reflect the heterogeneity of the primary Achaean gneiss.

The petrographic organization is similar from one sample to another in both profiles. Quartz is present in all samples, always fractured and sometimes filled with oxides, and displays sporadic dissolution features. Rare remaining micas (always partially kaolinitized) and anatase grains can also be observed. Secondary goethite, hematite and kaolinite booklets are always present. Iron oxide (sensu *lato*) septa are developed at the expense of dissolving fragmented quartz crystals. All these phases are spread within the typical lateritic matrix described in Nahon (1991), referred to as lateritic plasma.

Thin sections of Mananthavady reveal three broad types of petrographic structures: 1) samples with a significant content of secondary minerals (vermicules and oxides/oxyhydroxides) and remains of primary minerals (mainly rare micas and quartz) occurring inside a plasma, without any peculiar organization (Fig. 3a A); 2) samples with a majority of secondary minerals and remains of primary minerals with a partially preserved primary orientation (Fig. 3a B); 3) samples with a low content of primary and secondary minerals disseminated in a dominant plasma (Fig. 3a C). The structure of sample C1 960 is an exception as it consists in a pouch of massive kaolinite booklets and iron oxides (Fig. 3a D). The first two types of samples have petrographic weathering stage equivalent to the "phyllosilicate stage" described by Nahon and Colin (1982). The majority of the primary minerals have been replaced by kaolinite and the insepic matrix is not dominant. The last two samples have important insepic matrix content and non-negligible quantity of well crystallized iron oxyhydroxides. Their petrographic weathering stage is close to the "oxi-hydroxides" stage described by Nahon and Colin (1982). This is indeed characterized by the replacement of kaolinite by amorphous iron oxide/hydroxides which are further replaced by crystallized minerals of the same family.

The Payoddu samples can also be divided in three groups of petrographic organization. The B60 sample displays abundant iron oxide septa and fragmented quartz (Fig. 3b A) spread into a homogeneous lateritic plasma strewed by a significant porosity. The C1 and C1g horizons (Fig. 3b B) have large quantities of secondary and primary minerals

Table 1
Mineralogical composition of samples determined using XRD patterns.

Name	Horizon type	Thin section	Quartz	Goethite	Kaolinite	Gibbsite	Chlorite	Hematite	Anatase
MA A 30	A		XXX	X	XX	x	x	x	x
MA B 70	B	X	XXX	X	XX	x	x		x
MA Bca 120	BC		XX	X	XXX	x	x		x
MA Bca 200	BC		X	X	XXX	x	x		
MA BCb 270	BC1		X	XX	XXX	x			
MA C1 370	C1	X	XXX	X	XXX	x			
MA C3 470	C3		X	XXX	XXX				x
MA BCb 470	BC1		X	XX	XXX				
MA BCc 540	BC2	X	X	XX	XXX				
MA C2BC2 630	C2		XXX	X	XX			x	
MA C1 680	C1	X	XX	X	XXX			x	
MA C2BC2 740	C2		X	X	XXX				
MA C3 830	C3	X	X	XXX	XX				
MA C2d 950	C2d	X	XXX	X	X			x	
MA C1 960	C1	X	X	XX	XXX				x
MA C3C2 960	C2C3	X	XXX	X	XXX			x	
PA B60	B	X	XX	X	XXX		x	x	
PA BCg 130	BCg	X	XXX	X	XXX		x		
PA C1 320	C1	X	XXX	X	XXX			x	
PA C2 660	C2	X	XXX	X	XXX			x	

spread inside the lateritic plasma without any peculiar organization. These samples are poorer in septa and more porous than the other thin sections.

The low amounts of kaolinite booklets in both cases highlight the advanced "oxi-hydroxide" petrographic weathering stage described by Nahon and Colin (1982). The C2 horizon (Fig. 3b C) is characterized by a succession of two peculiar petrographic organizations. One is similar to that observed in the C1 and C1g horizons, rich in fragmented quartz, and the other corresponds to a kaolinite pouch structure, as observed in the Mananthavady C1 960 samples, also rich in fragmented quartz.

5.1.2. Regoliths geochemistry

5.1.2.1. Weathering Index and mass balance calculations. Long-term elemental fluxes have been investigated through mass balance calculations as described by Braun et al. (2012) in order to better apprehend the weathering processes affecting the profiles. This approach is based on the works of Brimhall et al. (1991) and Oh and Richter (2005): the mass of the weathered material is equal to the mass of the parent rock added to the mass of an element moving in (accumulation) or out (leaching) of the system.

The volumetric strain index $\varepsilon_{i,w}$ between the weathered material and the parent rock is estimated by:

$$\varepsilon_{i,w} = \left(\frac{\rho_p C_{i,p}}{\rho_w C_{i,w}} \right) - 1 \tag{2}$$

where, ρ is the bulk density in $g \cdot cm^{-3}$ obtained by the paraffin method and C_i is the chemical concentration of an immobile element. The indices p and w correspond to the parent and weathered materials respectively. Note that values around 0 indicate isovolumetric weathering, positive values indicate a volume increase and negative values a volume decrease between the weathered material and the parent rock (Braun et al., 2012). The typical error of this type of calculation is 20%.

Mass fraction transport function can be calculated for each element:

$$t_{j,w} = \left(\frac{\rho_w C_{j,w}}{\rho_p C_{j,p}} \right) (\varepsilon_{i,w} + 1) - 1 \tag{3}$$

where C_j is considered as element concentration. Note that if this function is equal to 0, the element is immobile during the weathering. A positive value induces a mass gain in the element and a negative value a loss between the regolith and the parent rock.

In the present study, zirconium is used as an "inert element" for the mass balance calculations because it is commonly described as immobile during saprolitization and ferralitization processes under tropical weathering (Braun et al., 2012 and ref. therein). In Mananthavady, the resulting values of ε_{Zr} can be divided in two parts: 1) the samples at the top of the profile, as well as MA C1 370 (a saprolite "pouch"), are characterized by a collapse ranging from 14 to 54% (see Table 2); 2) the other samples are characterized by a volumetric gain ranging from 8% to 168%. The same observation can be made in the Payoddu samples, the two samples at the top of the profile are shrinked when the other experienced a volumetric gain. Several factors can explain the collapse of the bottom part of this profile such as pedogenic activity linked to bioturbation shrinkage and to the replacement of primary and secondary minerals by an insepic matrix (Brimhall and Dietrich, 1987). The volumetric gain of the saprolite is less straightforward to explain. Expansion of biotite in its first weathering stage (Brantley, 2010 and ref. therein), can slightly contribute to this gain. It could also be depending on the specificities of zirconium (Zr) distribution arising from some degree of (unexpected) mobility (e.g. Beauvais, 2009) or from the mineralogical and chemical variability of the parent rock. For comparison, the same calculations have been done for Th (Supplementary File 3A), leading to an almost constant shrinking of ca 90%.

The chemical analyses are reported in the Supplementary File 3A. The transport functions of major elements are quite complex in Mananthavady (Fig. 4A): an apparent succession of preferential leaching/accumulation areas occurs along this laterite profile. Silicon is almost constantly leached, except in two saprolite samples. Silicon is particularly leached in the middle of the saprolite zone and at the bottom of the mottled zone. Iron and aluminum (Fe and Al) follow similar trends: they are both leached at the bottom of the saprolite zone as well at the bottom of the mottled zone. Fe and Al are also leached in the topsoil but accumulate otherwise. Alkaline and alkaline earths (Ca, Na, Mg, K) are always leached except in one sample of the topsoil that accumulates all of them. In the Payoddu profile (Fig. 4B), Si, Al and Fe follow similar trends with leaching in the topsoil and accumulation at the top of the saprolite while Ca, Na, Mg and K are all continuously leached.

Chemical index of alteration (CIA) is calculated from the Al_2O_3, CaO, Na_2O and K_2O content of samples (see Nesbitt and Young, 1982 for further information) in both profiles (Table 2). Except MA B70, all are significantly weathered, having values very close to the ideal kaolinite (CIA around 100). However, mass balance calculations show that major elements can be preferentially leached/accumulated depending on the zone of the studied profiles. This can be interpreted as the influence of the primary rock heterogeneity as well as can be attributed to the
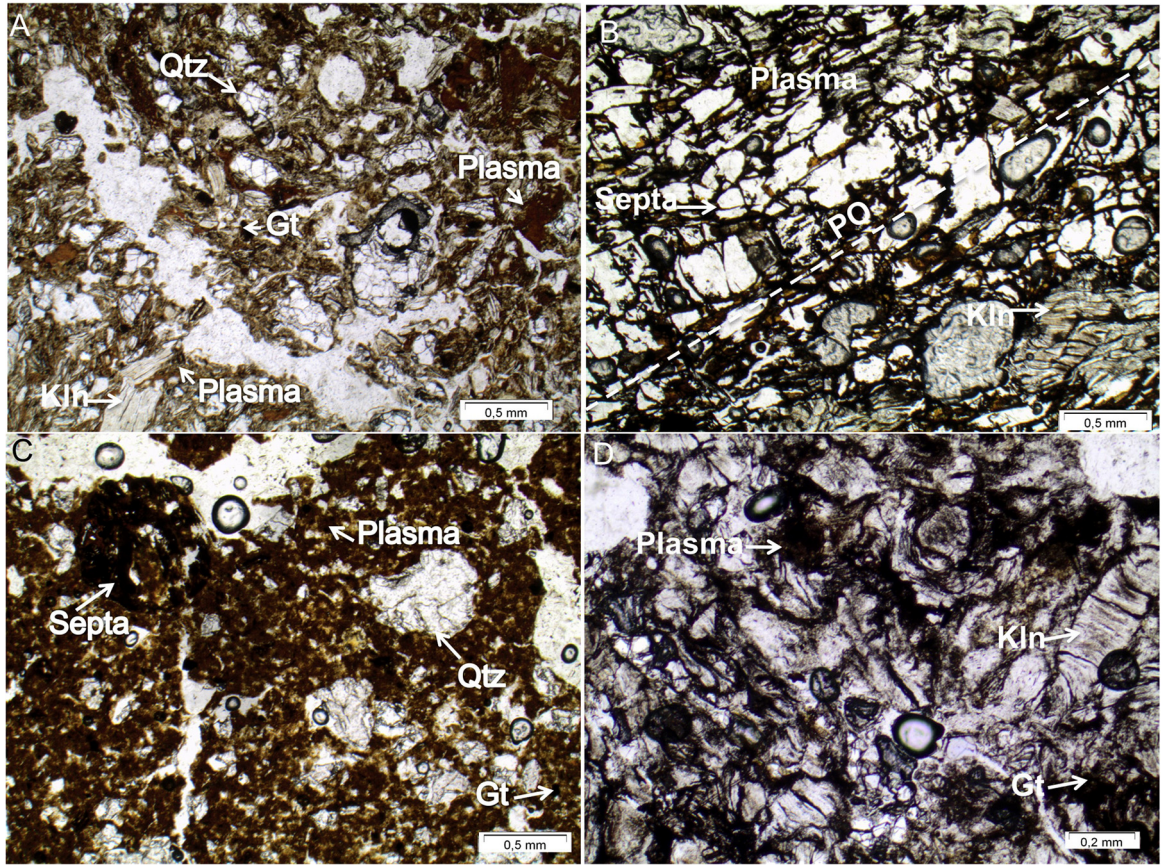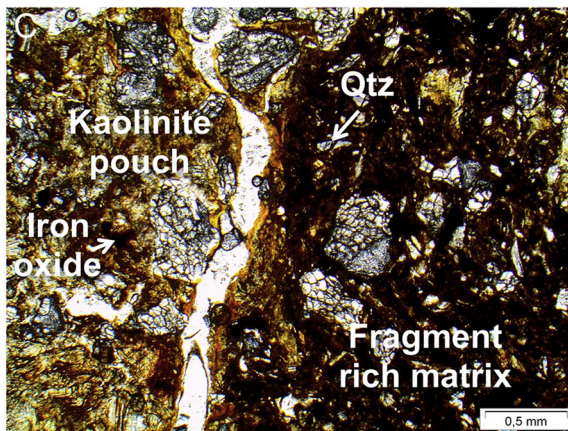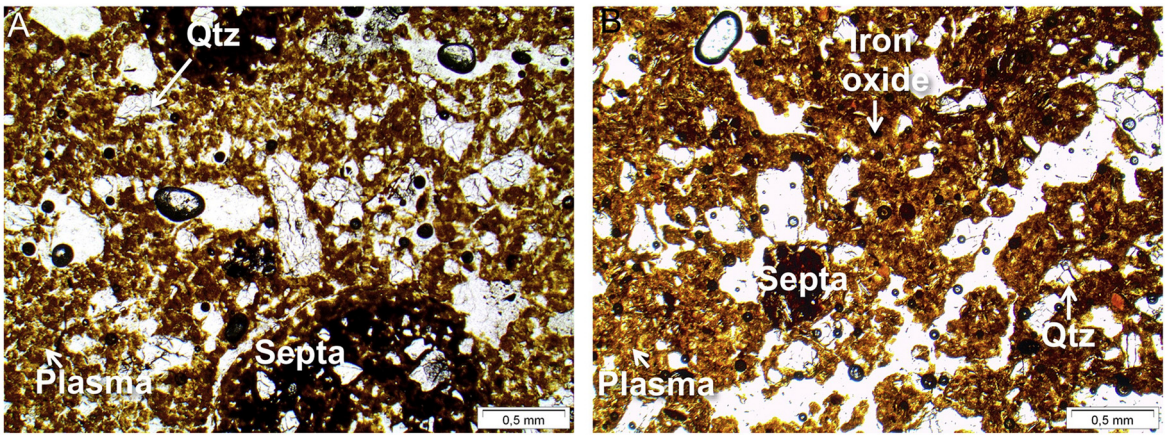
influence of several weathering fronts that could have only affected the rocks parts the most favorable to fluid circulation. The lack of correlation among the trends observed for different chemical elements suggests that the observed variations cannot be solely explained by a heterogeneous primary distribution of zirconium, the reference immobile element.

The variation of weathering intensity between the samples is confirmed by reporting the chemical compositions on a SiO_2-Al_2O_3-Fe_2O_3 ternary diagram (Fig. 5). This approach highlights three points: 1) soil samples can be divided in two groups, one, with samples located near the parent rock composition and the other located near the "advanced lateritization composition line" (i.e. samples composed by only kaolinite and iron oxides); 2) the various groups of samples (soil, mottled zone, saprolite and Payoddu) do not define a single chemical evolution trend; 3) the Payoddu samples are all regrouped around the parent rock composition except PA C2 660. In Mananthavady, some domains of the regolith appear to be more weathered than others although these variations do not display a simple relation with the soil structural horizons observed on the field. The non-negligible percentage of primary quartz in each sample can explain their important SiO_2 content (Supplementary File 2).

As a complementary test, WIS calculations (Meunier et al., 2013) have been performed (Supplementary File 3B, C and D). However, the WIS data hardly discriminate chemical weathering stages because of the strong lixiviation of monovalent and divalent cations. In addition, the higher concentrations in monovalent and divalent cations observed in three Mananthavady samples could also result from the heterogeneity of the primary Archean gneiss.

5.1.2.2. Distribution and mobility of radioactive elements. The EPR dating methodology is based on the assessment of radiation dose rate for each sample. The dose rate depends on the natural radioactivity resulting from the ^{238}U, ^{235}U, ^{232}Th decay chains and ^{40}K. A particular attention must be paid to the evolution of the concentration of these elements throughout the profile and to their spatial distribution (spread within the matrix vs concentrated in radioactive minerals). Indeed, the contribution to the clay matrix irradiation of radioactive elements contained in minerals with larger grain size can be limited by the relatively short mean free path of alpha particles (typically around 20 μm in silicates).

The chemical compositions (Table 3) show that both Uranium (U) and Thorium (Th) accumulate from the parent rock (around <0.03 ppm for U and 0.12 ppm for Th) to the top of the profile (1.5 ppm for U, 7.07 ppm for Th in Mananthavady and 1.32 ppm for U, 4.46 ppm for Th in Payoddu). It is commonly considered that Th is an immobile element due to the very low solubility of thorianite (ThO_2) (Langmuir and Herman, 1980). In contrast, oxidized U species usually display a higher mobility in supergene environments (Langmuir, 1978). The U accumulation in the investigated profiles can be linked to the presence of resistant U-bearing minerals, such as zircon, or to a mobility limited by adsorption on finely divided clays and oxide minerals.

Mass balance calculations based on zirconium (Fig. 6A, B), indicate that the accumulation of U and Th does not follow any regular trend from the saprolite to the topsoil in Mananthavady. The lack of correlation between Zr and Th, with possible preferential accumulation/leaching zone within this profile, could be partially explained by the impact of the complexity and heterogeneity of the gneissic parent rock on the Th mass balance calculations. An unexpected slight mobility of Zr

may also partially explain this phenomenon (e.g. Beauvais, 2009). However, the U accumulation could also be explained by the fact that U is mainly adsorbed on the matrix minerals (see below) and not located in weathering-resistant minerals. In Payoddu, there is a clear increase of U and Th concentrations toward the surface of the profile. Note that the similar evolution of U and Th concentrations within each profile is confirmed by the mass balance calculations based on Th, which indicates a low variability of U compared to the Th content in all profile (Supplementary File 3A).

To estimate the proportion of U content in U-bearing minerals or spread in the matrix, induced fission track mapping has been performed on 5 samples of Mananthavady (B 70, BCc 540, C 1680, C3 830 and C1 960) and on 3 samples of Payoddu (B60, BC1g 130 and C2 660). This methodology allows determination of the spatial distribution of uranium at the micrometer scale, despite the relatively low concentration of this element (around 1 ppm and below). Each of these samples is representative of one of the types of petrographic organization described in Section 5.1.1. In addition, a topsoil sample of the Mananthavady profile (B 60) was added to the series.

The distribution of fission tracks is similar for 6 of the 8 samples (see table Supplementary File 5 and 6). The fission tracks (Supplementary File 4) are (i) spread homogeneously or (ii) clustered around some hot spots displaying between 10 and 150 tracks, reflecting the distribution of U between the clay matrix and U-bearing minerals (see Supplementary File 4 and 5). The rare U hot spots observed in each thin section (excluding PA C2 660) correspond to local concentration of 3.41 to 685 ppm of uranium, with an average of 262 ppm. As they represent at most 0.174% of the counted areas, this means that <10% of total U is trapped in U-bearing minerals (Supplementary File 6). The lateritic matrix contains between 0.134 and 1.11 ppm U with an average value of 0.39 ppm U. This represents more than 90% of the total U, based on its important relative area compared to the rare U-bearing minerals. In the MA C1 960 sample (kaolinite pouch), fission track analysis indicates that 24.2% of total U is concentrated in U-bearing minerals. Those observations confirm the hypothesis that U is mainly spread inside the lateritic matrix of the samples for both soil profiles. This element is likely immobile in present-day conditions, adsorbed on small oxide and phyllosilicate surfaces. According to the similar mass balance results (i.e. no regular accumulation) and to the difficulty to detect Th-bearing phases in our samples, it is assumed that Th is also homogeneously distributed inside the matrix. These data allow a first correction of the dose rate. For the uranium rich minerals with large grain size, the alpha contribution is not considered because it only affects a thin rim around their surface and not the bulk kaolinite sample. For the matrix, the whole U and Th dose rates are considered.

Another correction of dose rate can be considered. It is related to the opening of decay chains. Losses of radioactive daughter elements are commonly observed in regolith open systems (Dequincey et al., 2002; Balan et al., 2005; Chabaux et al., 2011). Radon (Rn), a mobile noble gas with an important capacity of diffusion, and radium, that can form water-soluble complexes, are often described as common sources of disequilibrium of the U and Th decay chains (Oczkowski et al., 2000 and references therein). Rn loss intensity varies with bedrock, soil moisture, soil type and mineralogy (Benke and Kearfott, 2000; Oczkowski et al., 2000 and references therein; Sakoda et al., 2011). The actual impact of these losses on the dose rate is difficult to assess but a total opening of the system with subsequent total leaching of Rn is unlikely. In some rare humid soils, clay-rich soils and/or soils developed on gneissic rocks, Rn loss up to 40% has been reported (Sakoda et al., 2011).

Fig. 3. a: Thin section photomicrographs from Mananthavady samples. A) C1 680, primary and secondary minerals rich sample showing that fractured quartz, goethite, kaolinite booklet, rare hematite and kaolinitized micas fragments are spread into minor plasma. B) C3 830, sample with the parent rock petrographic organization preservation showing that septa and kaolinite vermicules have a preferential orientation (PO). C) B 70, a matrix rich sample showing that the secondary minerals are present with some primary relics (mainly fractured quartz) and septa within the plasma. D) C1 960, sample containing a kaolinite pouch. b: Thin section photomicrographs from Payoddu samples. A) B60 sample, septum and fragmented quartz rich sample showing that they are both spread into the plasma. B) C1 320, fragmented quartz and oxides rich sample, both spread into a porous matrix. The C1g 130 has the same petrographic organization. C) C2 660, a kaolinite pouch and fragmented quartz rich area can be identified. Kln: Kaolinite; Gt: Goethite, Qtz: Quartz, Diss: Dissolution zone, Gt F: Goethite formation, PO: preferential orientation.
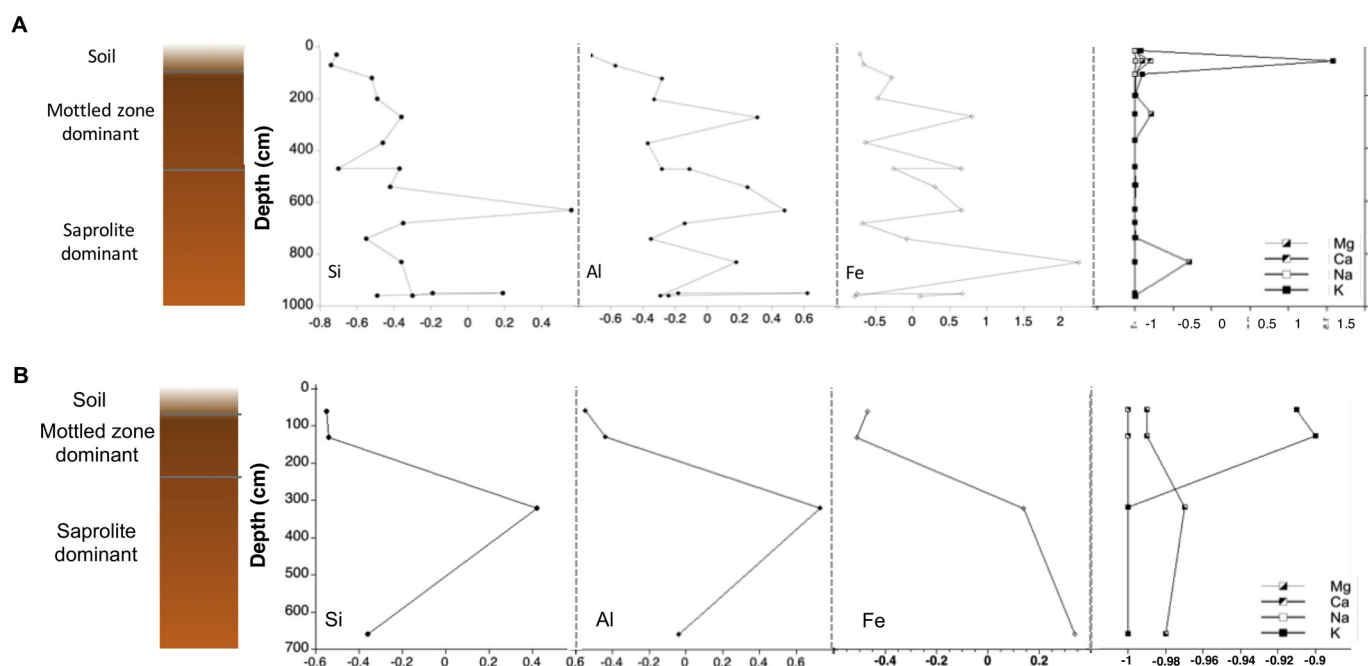
Fig. 4. Mass fraction transport function (τ) of major elements as a function of depth in the Mananthavady profile (A) and Payoddu profile (B).

However, according to these authors, Rn loss can be as low as 3% in a compact indurated laterite. In absence of data about Rn concentrations, the hypothesis of a partial opening of the system due to a radon loss was assumed at the maximum value of 40% of Rn loss for both U and Th decay chains. This assumption allowed a second correction of the dose rate which maximized the value of the age.

5.2. Identification of kaolinite generations and EPR dating

5.2.1. Structural disorder of kaolinites

The production rate of radiation induced defects (RID) in kaolinite has been shown to depend on its degree of structural disorder (Allard et al., 1994; Allard and Muller, 1998). Accordingly, the structural order of kaolinite samples can be used to define groups of samples which are expected to display a similar behavior under ionizing radiations. Among various techniques, structural order parameters can be obtained from the EPR signal of structural iron (Gaite et al., 1997; Allard and

Muller, 1998) or from the Mid-infrared spectrum of OH stretching modes (Farmer, 1974; Russel and Fraser, 1994; Lucas et al., 1996; Gaite et al., 1997; Balan et al., 2007).

EPR of structural trivalent iron, i.e. substituting for Al^{3+} in the kaolinite structure, is a sensitive method to distinguish kaolinite families based on their crystalline disorder. The corresponding spectrum mostly occurs around $g = 4.3$, i.e. at low magnetic field (Figs. 7A and 8). Two superimposed structural iron spectra are observed in this area: 1) the $Fe^{3+}_{(I)}$ isotropic spectrum, characterized by a signal near $g = 4.19$; 2) the $Fe^{3+}_{(II)}$ spectrum, characterized by signals at $g = 8.62$, 4.71 and 3.69 (Balan et al., 1999; Balan et al., 2000, 2007). The relative intensity of these two spectra can be used as a proxy for kaolinite structural disorder: the more intense the $Fe^{3+}_{(I)}$ signal, the higher the kaolinite local structural disorder. The $Fe^{3+}_{(II)}$ signals, in turn, characterize well-ordered structure. In the infrared spectra, the variations of band shape and intensity related to OH-stretching modes (3600 to 3750 cm^{-1}) in the mid-infrared (MIR) region can also be used to further characterize

Table 2
Table with the results of the volumetric strain (ε), chemical index of alteration (CIA) and open system mass fraction transport (τ) calculations.

Samples	τ_u	τ_{Th}	τ_K	τ_{Si}	τ_{Al}	τ_{Fe}	CIA	ε_{Zr}	Bulk density
MA A 30	5.28	12.77	−0.93	−0.71	−0.72	−0.71	100	−0.54	1.55
MA B 70	7.29	16.80	1.58	−0.74	−0.57	−0.66	77	−0.38	1.46
MA BCa 120	10.08	28.63	−0.91	−0.52	−0.28	−0.28	101	0.00	1.40
MA BCa 200	6.37	45.56	−1.00	−0.49	−0.33	−0.47	101	−0.16	1.58
MA BCb 270	12.31	26.51	−1.00	−0.36	0.31	0.80	101	0.78	1.35
MA C1 370	3.49	18.53	−1.00	−0.46	−0.37	−0.64	101	−0.14	1.48
MA C3 470	7.67	12.82	−1.00	−0.70	−0.28	0.66	103	0.33	1.09
MA BCb 470	6.08	25.06	−1.00	−0.37	−0.11	−0.26	101	0.21	1.39
MA BCc 540	4.89	13.60	−1.00	−0.42	0.25	0.30	101	0.66	1.27
MA C2 BC2 630	7.90	8.02	−1.00	0.56	0.48	0.66	102	1.62	1.46
MA C1 680	2.28	36.56	−1.00	−0.35	−0.14	−0.68	101	0.22	1.27
MA C2BC2 740	4.94	18.82	−1.00	−0.55	−0.35	−0.08	104	0.08	1.30
MA C3 830	11.33	18.05	−1.00	−0.36	0.18	2.24	104	1.68	1.10
MA C3C2 960	3.72	53.30	−1.00	−0.30	−0.29	−0.78	101	0.07	1.40
MA C2d 950	5.90	1.31	−1.00	0.19	0.62	0.67	102	1.39	1.37
MA C1 960	5.95	12.58	−1.00	−0.49	−0.24	0.10	102	0.21	1.31
PA B 60	7.61	12.48	−0.91	−0.55	−0.55	−0.47	101	−0.22	1.42
PA BC1g 130	5.86	11.43	−0.90	−0.54	−0.44	−0.51	100	−0.16	1.39
PA C1 320	3	5.18	−1.00	0.42	0.73	0.14	101	1.25	1.53
PA C2 660	1.72	4.00	−1.00	−0.36	−0.04	0.34	102	0.6	1.22
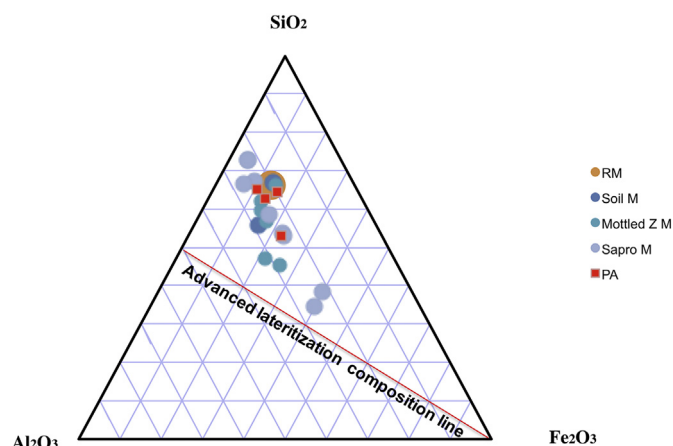
Fig. 5. Ternary Al_2O_3-Fe_2O_3-SiO_2 diagrams for different parts of the regoliths of Mananthavady and Payoddu. The advanced lateritization composition line (only kaolinite and iron oxides as main component of the soil) is indicated. With: RM: parent rock; Soil M: Mananthavady soil samples; Mottled Z M: samples of the Mottled zone of the Mananthavady profile; Sapro M: Mananthavady saprolite samples and PA: samples of Payoddu.

the kaolinite families identified using EPR spectroscopy. Well-ordered kaolinites present well-defined 3668 cm^{-1} and 3652 cm^{-1} bands on FTIR spectra.

In Mananthavady, the 16 purified samples can be categorized in 5 groups with similar EPR and IR spectra (Fig. 8), referred to as "kaolinite disorder families" (Supplementary Files 7 and 8). The distinction between families is less straightforward using FTIR spectra than EPR spectra (Fig. 8a A, B). The first (F1), represented by the MA C1 680 sample, is characterized by an EPR spectrum dominated by the $Fe^{3+}_{(II)}$ signal and well-defined MIR stretching bands, with apparent amplitude of the 3668 cm^{-1} band higher than that of the 3652 cm^{-1} band. These spectra are characteristic of well-crystallized kaolinites. The last family (F5), represented by the MA C2d 950 sample, is on the contrary characterized by a high intensity of the $Fe^{3+}_{(I)}$ signal that strongly modifies the EPR spectrum shape. It is also characterized by broad IR bands at 3668 and 3652 cm^{-1}. These observations are characteristic of disordered kaolinites. The three other families display intermediate characteristics between these two end-members, as attested by their EPR and FTIR spectra (Fig. 8).

The 4 Payoddu purified samples (Fig. 8b A and B) display EPR and MIR spectra in the OH-stretching region characterizing different structural kaolinite order. The PA C1 320 sample is similar to the F1 family of Mananthavady with spectra of well-ordered kaolinites whereas the PA B60 sample displays EPR and IR spectrum characteristic of more disordered kaolinites, but still more ordered than the F4 and F5 kaolinites previously described. The other studied samples are transition steps between these two end-members. Note that kaolinites from Payoddu are relatively well ordered.

The kaolinite disorder families are not correlated to sampling depth in both laterite profiles (Table 3) but likely correspond to local variations of prevailing physico-chemical conditions and/or to a complex weathering history.

5.2.2. EPR spectra of radiation-induced defects in the Mananthavady and Payoddu kaolinites

In addition to the structural iron with a signal around g = 4.3, the EPR spectra of kaolinite samples (Fig. 7a), exhibit a paramagnetic signal around g = 2 assigned to radiation induced defects (RID). This signal is superimposed to a broad signal due to remaining superparamagnetic iron-rich phases or domains. Indeed, several vermicular kaolinite layers partially pseudomorphosed by iron oxides can be observed in the samples (Supplementary File 9) and could have been partially protected from the selective dissolution (CDB) procedure. The RID signal is anisotropic and usually displays two components at $g_{//}$ = 2.049 and $g_{\perp}$ = 2.008, corresponding to the dominant A-center signal (Clozel et al., 1994). The signal of Mananthavady samples is unusual (Fig. 7b). Only a weak signal at the $g_{\perp}$ position is visible (Figs. 7, 9). The $g_{//}$ component is not apparent on the EPR spectra of these samples and only appears when increased because of artificial irradiation (from 0 to 2342 kGy). The growth of the signal as a function of radiation dose (Fig. 9) confirms that the weak $g_{\perp}$ signal corresponds to a kaolinite RID signal. Its low intensity indicates a low concentration of A-type RIDs in the investigated kaolinite purified samples. This can be due to young ages of these minerals and/or to low natural radiation dose rates.

5.2.3. Determination of paleodoses

The relation between the concentration of RID (derived from the intensity of the corresponding signal) and the paleodose, i.e. the radiation dose experienced by kaolinites since their formation, was determined using artificial irradiation experiments and by fitting the dosimetry

Table 3
Summary of dating results. The names of artificially irradiated samples are underlined and reported in italics.

| Name	Horizon type	Disorder family	RID intensity (AU)	Paleodose (kGy)	U (ppm)	Th (ppm)	K (%)	Dose rate (kGy/ka)	Dose rate corrected (kGy/ka)	Age (Ma)
MA A 30	A	F4	1.744	20.299	1.5	7.07	0.12	0.0104	0.007805	2.60$_{\pm 2.72}$
MA B 70	B	F4	3.4920	40.698	1.57	7.26	3.38	0.0135	0.01142	3.56$_{\pm 1.47}$
MA Bca 120	BC	F4	2.72	23.564	1.36	7.82	0.084	0.0105	0.00789	2.99$_{\pm 1.14}$
MA Bca 200	BC	F3	2.14	35.597	0.95	12.84	<LD	0.0132	0.01000	3.56$_{\pm 1.31}$
MA BCb 270	BC1	F4	2.136	46.067	0.95	4.22	<LD	0.00629	0.00468	9.83$_{\pm 3.74}$
MA C1 370	C1	F1	0.3277	4.076	0.6	5.62	<LD	0.00636	0.00478	0.85$_{\pm 0.89}$
MA C3 470	C3	F2	0.4744	4.7719	1.02	3.51	<LD	0.00593	0.00448	1.07$_{\pm 1.12}$
MA BCb 470	BC1	F1	0.366	4.56	0.72	5.71	<LD	0.0068	0.00510	0.89$_{\pm 0.94}$
MA BCc 540	BC2	F4'	0.173	5.31	0.48	2.56	<LD	0.00352	0.00265	2.00$_{\pm 0.76}$
MA C2BC2 630	C2	F5	0.484	5.894	0.4	0.87	<LD	0.00192	0.00144	4.08$_{\pm 4.28}$
MA C1 680	C1	F1	0.3845	7.8453	0.36	8.89	<LD	0.00827	0.00627	1.25$_{\pm 0.47}$
MA C2BC2 740	C2	F4'	1.83	44.156	0.72	5.19	<LD	0.00636	0.00483	9.135$_{\pm 3.46}$
MA C3 830	C3	F2	0.282	3.008	0.72	2.38	<LD	0.0132	0.00310	0.97$_{\pm 0.37}$
MA C2d 950	C2d	F5	0.63	8.613	0.36	0.26	<LD	0.0013	0.00098	8.82$_{\pm 3.41}$
MA C1 960	C1	F4'	1.548	30.197	0.75	3.16	<LD	0.00482	0.00332	9.1$_{\pm 9.53}$
MA C3C2 960	C2C3	F1	0.1746	2.159	0.54	13.33	<LD	0.0124	0.00943	0.229$_{\pm 0.24}$
PA B60	B	F2p	3.167	42.536	1.32	4.46	0.08	0.00769	0.00567	7.49$_{\pm 2.84}$
PA BC1g 130	BCg	F1p	2.49	20.178	1	3.9	0.09	0.00627	0.00478	4.22$_{\pm 1.6}$
PA C1 320	C1	F3p	2.549	30.221	0.2	0.65	0	0.00113	0.000858	38.06$_{\pm 14.46}$
PA C2 660	C2	F4p	2.83	46.622	0.24	0.94	0	0.001487	0.001144	40.73$_{\pm 15.47}$
Archean Gneiss	/	/	/	/	<L.D.	0.12	0.19		/	/
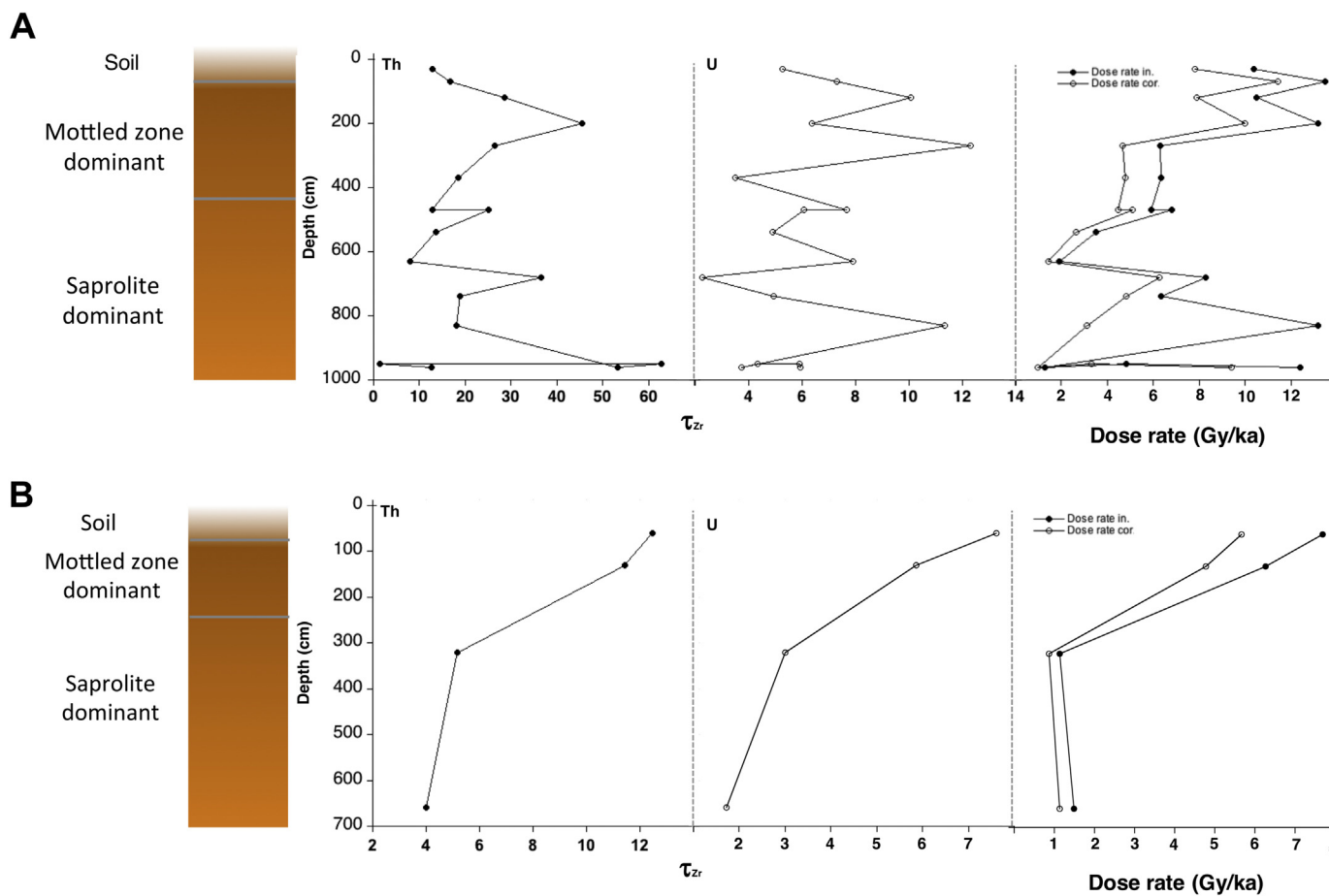
Fig. 6. Evolution of the U, Th mass fraction transport function (τ) with depth in the Mananthavady profile (A) and the Payoddu profile (B) compared with the evolution of the sample dose rates (cf Section 5.2.4). With in: initial and corr: corrected.
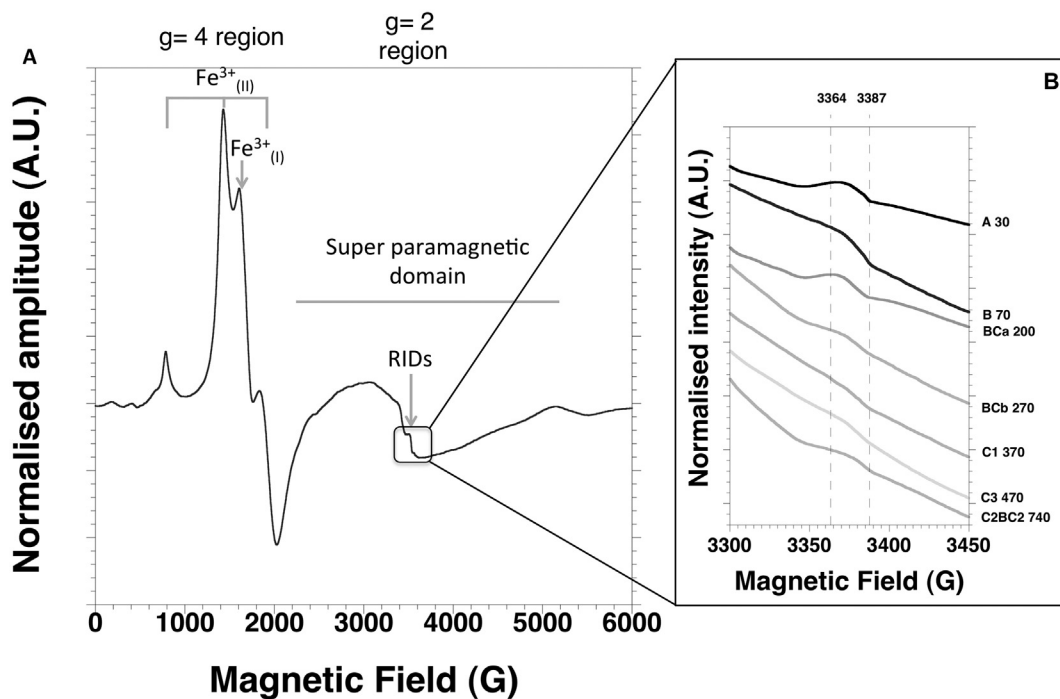

Fig. 7. Mananthavady kaolinite EPR spectra at 110 K and enlarged view of the g = 2 zone for the main samples families. The natural samples RID signals have a very low intensity.
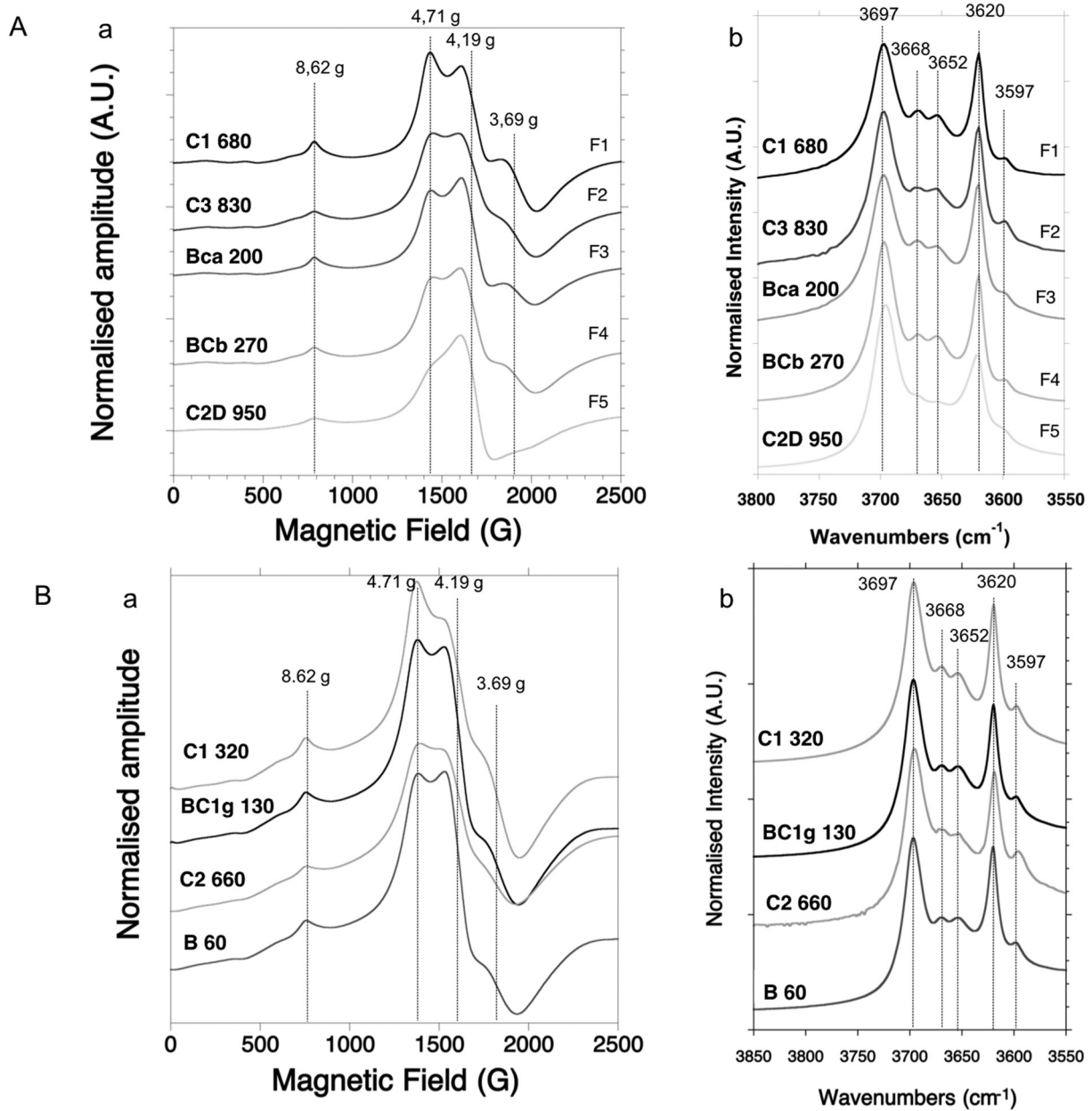
Fig. 8. Enlarged view of the EPR g = 4 zone (a) and of the IR OH-stretching (b) zone of characteristic samples from each structural disorder family. A: Samples from the Mananthavady profile (F1, F2, F3, F4 and F5). F1 displays the highest structural order and F5 is highly disordered. B: The 4 Payoddu samples.

curves by a simple exponential function (Allard et al., 1994; Allard and Muller, 1998; Balan et al., 2005). In some cases, a linear component was added to the exponential function (Duval, 2012), leading to the following general equation:

$$I = I\infty \times \left(1 - e^{-\mu(D+P)}\right) + Fl \times (D + P) \tag{4}$$

where I is the RID's concentration, I_∞ is the RID's concentration at saturation, μ is an efficiency factor, P is the natural paleodose, D is the artificial dose rate, and Fl is a linear factor explained in Duval (2012). For this study, ten purified samples (Table 3) were artificially irradiated in Mananthavady as well as all the Payoddu purified samples. All the parameters obtained from the modeling of dosimetry curves are presented in the Supplementary File 10.

Selected dosimetry curves and an enlarged view of low-dose parts are presented in the Fig. 10A, B for each Mananthavady kaolinite family

and Fig. 10C, D for the 4 Payoddu samples. It reveals that the F4 family should be divided in two subfamilies named F4 and F4′ one (Fig. 10A, B and Table 3), with different dosimetry curves. Based on the link between crystalline order and dosimetry parameters (Allard et al., 1994), the fitting parameters of a sample representative of each Mananthavady kaolinite family have been used to estimate the paleodoses of unirradiated members of the same family. These extrapolated paleodoses can however only be considered as an estimation. They will indicate a wide period of formation of the kaolinite contained within the samples a contrario to the ones artificially irradiated that will provide a precise age of the dated kaolinite. The obtained paleodoses span over one order of magnitude, from 2.15 to 46.62 kGy (Table 3). The relative uncertainty on paleodoses is estimated at 36% due to the combined errors on RIDs concentrations and curve fitting. Note that the relative uncertainties on paleodoses for the unirradiated samples are larger (see Table 3 and Supplementary File 11 for further information). As a result, two samples, the MA A 30 and MA C1 960

samples, with relatively high paleodoses and very large error bars were not considered further in this study.

5.2.4. Dose rate determination

The paleodoses recorded by natural kaolinites result from the additive contribution of α, β and γ emissions of the natural radioactive decay chains (^{238}U, ^{235}U, ^{232}Th) and of ^{40}K. The corresponding dose rate values have been calculated using relation between dose rates and concentration of radioactive isotopes provided by Adamiec and Aitken (1998) for closed systems at the secular equilibrium. The dose rate arising from cosmic rays has been considered negligible. The concentration of radioactive elements in the samples are low compared to other studied lateritic regoliths (see e.g. Dequincey et al., 2002; Balan et al., 2005): U ranges from 0.2 to 1.57 ppm, Th from 0.26 to 13.33 ppm and K is only detectable in top profile samples with contents from 0.08 to 3.38% (Table 3). The corresponding uncorrected dose rates vary over one order of magnitude, from 1.13 to 13.5 Gy/ka (Table 3), with a calculated uncertainty varying between 6 and 12% (see the SARM error analysis http://www.crpg.cnrs-nancy.fr/SARM/index.html). Uncorrected ages of the samples can be obtained from these values (Supplementary File 6). Adamiec and Aitken (1998) also proposed values of dose rate in case of 100% radon escape. As discussed above, a partial radon loss of 40% has been considered in this study. This assumption will correspondingly lower the dose rate due to U- and Th-decay chains. The corrected dose rate was calculated by using the secular equilibrium dose rate values for 60% of U and Th concentration and of the dose rates with total radon escape for 40% of the U and Th.

In addition, the alpha contribution to the dose rate of U-bearing minerals with large grain size is reduced, due to the limited free path of alpha particles in silicates (~20 μm). As explained above, the mapping of fission tracks shows that <10% of the U is present inside U-bearing minerals and more than 90% is spread in the matrix (except sample MA C1 960). Accordingly, the alpha contribution to the U dose rate has been simply lowered by 10% for all samples, except MA C1960. Because it has been assumed that Th is homogeneously distributed, no correction has been applied for this element. The corrected dose rates range between 0.8 and 11.42 Gy/ka (Table 3, Figs. 6, 11).

At last, the relative enrichment in U and Th relative to other more mobile elements could have caused a progressive increase of the dose rate through geological time, particularly for the mottled zone and the soil. However, this phenomenon is particularly difficult to assess for old kaolinite populations (several millions of years) as all available accumulation models were calibrated for time scales of <1 Ma (Dequincey et al., 2002). For younger kaolinite populations, it is expected to have a limited influence on the dose rate, assuming that U and Th enrichments are relatively slow processes. As a consequence, it has not been considered in the present study.

5.2.5. Kaolinite ages

The isochronal relation between the dose rate and the paleodose is linear (Fig. 11). Calculated kaolinite ages vary between 0.229 and 40.73 Ma (Table 3). They are organized into 4 groups with ages around 39 Ma (2 samples), 9 Ma (4 samples), 3.5 Ma (4 samples) and 1 Ma (7 samples). Because of its large paleodose error, the MA C2BC2 630 sample cannot be precisely connected to any of the age groups and has not been considered for the data interpretation. The MA BCc 540 sample has a quite narrow uncertainty but, still could not be included in the 1 or the 3.5 Ma group.

Due to the correction with maximal radon loss, these ages can be considered as maximal ages. However, uncorrected ages (i.e. with no radon loss, see Supplementary File 6) still occur within the incertitude range of the corrected ages, forming the same age groups. Only the corrected ages are considered in the following discussion.

6. Discussion

6.1. Kaolinite ages and evolution of lateritic profiles

Kaolinite is the main weathering silicate formed during the development of lateritic regolith. Several authors have described the evolution of kaolinite crystal chemistry along a lateritic profile, highlighting the coexistence of various generations of kaolinites within the same profile (e.g., Lucas et al., 1986; Muller et al., 1995; Girard et al., 2002; Nahon, 2003; Balan et al., 2005). The occurrence of generations of other secondary minerals within a single weathering profile has also been reported for Mn oxides (Vasconcelos, 1999; Beauvais et al., 2008; Bonnet et al., 2016) and iron oxides (e.g. Allard et al., 2018). These generations are currently interpreted as a clue of an episodic evolution of the weathering profile, with the formation of a large amount of secondary minerals coinciding with short weathering pulse induced by optimum climatic conditions (Vasconcelos, 1999; Retallack, 2010; Bonnet et al., 2016). These minerals will replace or hide the ones resulting from the less intense continuous weathering that prevail on continental surfaces.

In the present study, kaolinite is present in all the samples, displaying various degrees of crystalline disorder and ages. This confirms the existence of several generations of kaolinites within both Indian lateritic profiles. However, the distribution of kaolinite ages does not follow a regular trend with the sampling depth, differing from that reported for Brazilian laterites (Balan et al., 2005). Older kaolinites are found at the bottom of both profiles but the younger kaolinites are spread throughout the profiles, preventing to define trend with depth, particularly in Mananthavady (Supplementary File 12) samples. The 4 top-most samples in the Mananthavady profile display similar ages (i.e. around 3 Ma) whereas in Payoddu the top-most sample displays an age of 7.49 Ma. The younger kaolinites (i.e. the 1 Ma group) display similar lower structural disorder suggesting that they formed under similar geochemical conditions.

Two of the Payoddu samples have ages that can be regrouped with kaolinite age groups of the Mananthavady profile, confirming that both regoliths have experienced a similar history. It is noteworthy that both profiles also display a structural continuity from the complex folded saprolite to the topsoil: saprolite and soil horizons are particularly intricated (Fig. 2A, B). This structural observation indicates that the observed ages cannot be interpreted as being related to the presence of several distinct paleosols within each profile. In addition, there is no succession of A, B, C horizon sequences in the profiles, as would be expected with several paleosols.

The lack of general correlation between kaolinite age and disorder (Supplementary File 12) suggests that the kaolinite crystal-chemistry
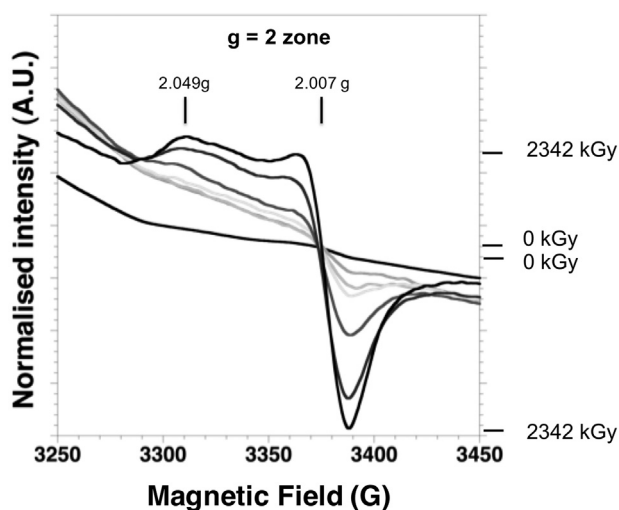

Fig. 9. Evolution of the RID signal (recorded at 110 K) of a purified sample as a function of experimental irradiation dose.
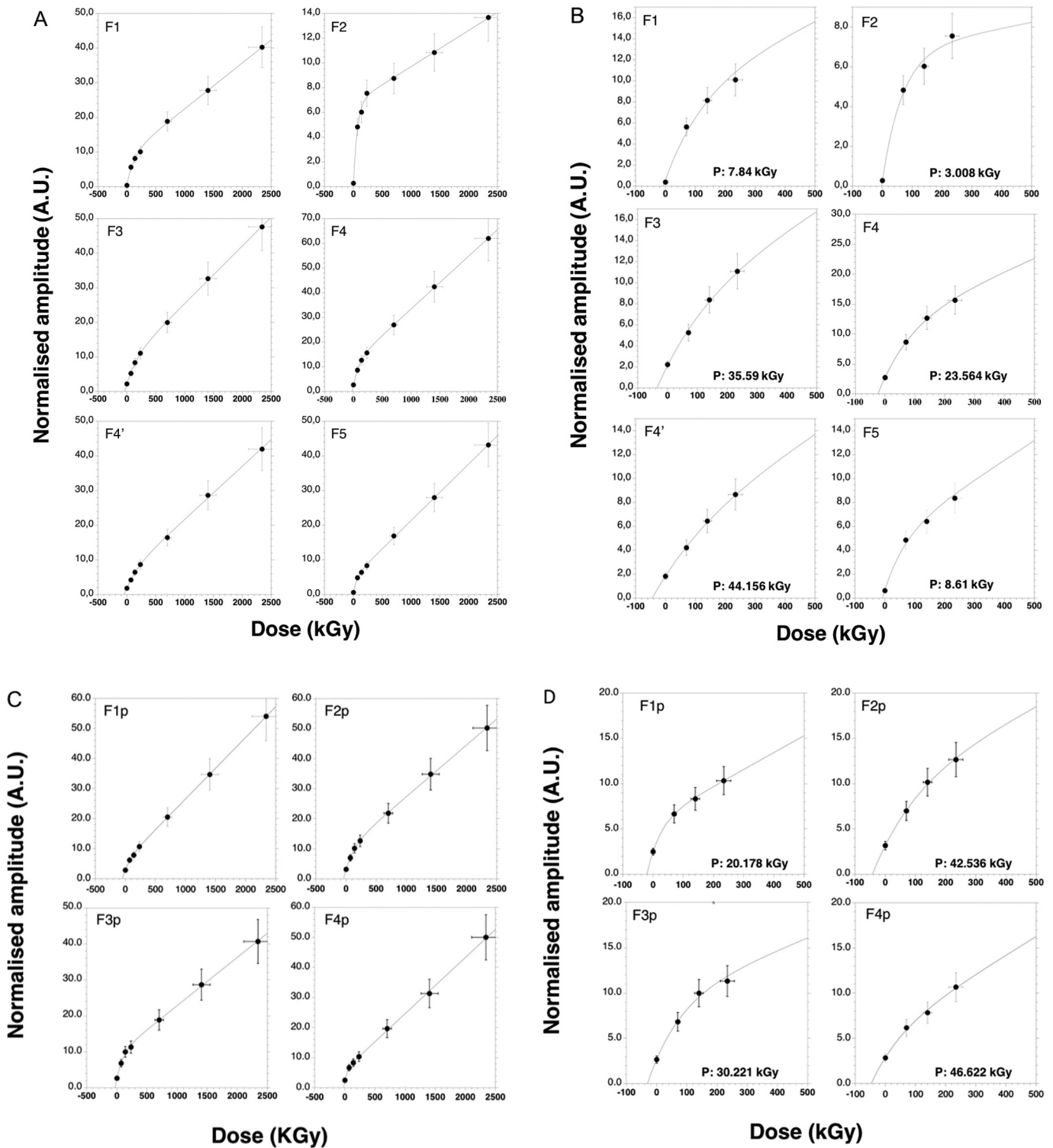
Fig. 10. A: Selection of the most representative dosimetry curve of each kaolinite disorder family for the Mananthavady samples, B: Enlarged view of the low-dose part of the Mananthavady dosimetry curves, C: Selection of the most representative dosimetry curve of each kaolinite disorder family for the Payoddu samples, D: Enlarged view of the low-dose part of the Payoddu dosimetry curves. The sample representing the F1 family is C1 680, it is C3 830 for the F2 family, BCa 200 is for the F3 family, BCa 120 for the F4 family, C2BC2 740 for the F4′ family, C2d 950 for the F5 family, BC1g 130 for the F1p family, B 60 for the F2p family, C1 320 for the F3p family, C2 660 for the F4p family.

most likely result from local physico-chemical conditions prevailing during their formation in soil microenvironments, consistently with the observation of Tardy (1993). As a matter of fact, the replacement of older kaolinites by younger ones through dissolution/recrystallization processes has been related to fluctuations of saturation degree of pore solutions with respect to kaolinite (Lucas et al., 1996 and references

therein). These fluctuations can be linked to vertical/horizontal moving weathering fronts but also to the channeling of water flow within a soil profile. Thus, the locations of youngest samples may correspond to preferential undersaturated-fluid paths during high precipitation periods. These paths are favored by the local porosity and could be linked to the parent rock heterogeneity. They could have also evolved in length and width
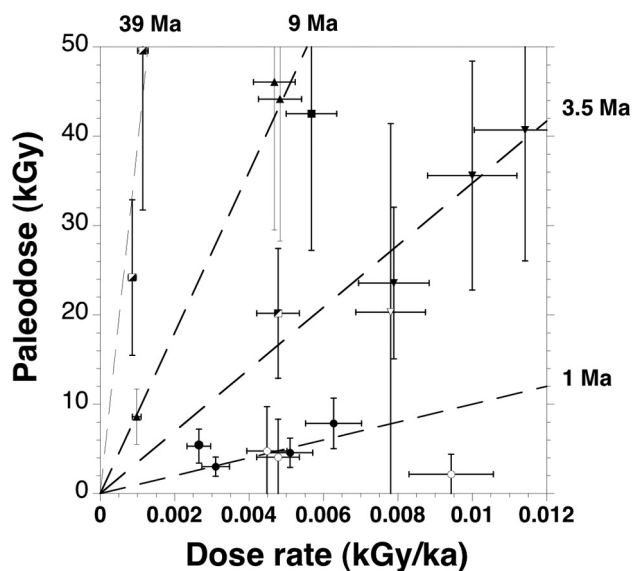
Fig. 11. Relation between the paleodose and dose rate of the Mananthavady and Payoddu samples. Four age groups can be observed around isochrons: one with almost contemporaneous samples (1 Ma), one with young samples (3.5 Ma), older samples (9 Ma) and one oldest group (39 Ma). The Mananthavady data are represented as circles, in black, for samples artificially irradiated and in white for those that correspond to extrapolated dosimetry parameters. The samples from Payoddu are represented with squares (all of them have been irradiated). Their filling patterns correspond to their age group.

during the profile history explaining the preservation of several generations of kaolinites. This preservation of old kaolinites from the saprolite can only be explained by the fact that microenvironment fluids of old phyllosilicate populations should be at saturation with their local mineralogy, as explained in Tardy (1993), and are likely preserved from the influence of percolating undersaturated solutions. Within the Mananthavady saprolite, the oldest kaolinites occur in samples with the weakest relative accumulation of aluminum, suggesting that these domains have been less leached than the others. However, this hypothesis is not confirmed by the Payoddu data in which an old sample (38 Ma) is linked to a significant aluminum concentration.

The lack of young kaolinite in topsoils can be interpreted as arising from important erosion, which can be correlated with high precipitations in this area and the location of these laterite profiles on hill slopes. The Payoddu laterite profile, located at the base of a hillslope, is more eroded than the Mananthavady one. This profile also contains the oldest relics of kaolinite at 10 m depth.

Overall, kaolinite dating shows that for the investigated lateritic profiles, there is no evidence of a simple vertical weathering history, the simplest model exhibiting the oldest samples at the top of the profiles and the youngest at their bottom. Instead, successive weathering processes have affected specific area of a laterite profile whereas other parts were preserved. This study thus exemplifies that old soft tropical weathering surfaces can display renewed domains, modified by recent weathering pulses, as well as significantly older relictual zones which are suitable for reconstruction of past environment.

6.2. Kaolinite ages as record of paleoclimatic variations

As discussed by Vasconcelos (1999), secondary minerals of laterites can be used to discriminate weathering pulses linked to specific climatic conditions. Indeed, even if these minerals can form under continuous weathering, such pulse will cause the formation of large quantity of these minerals. The observation within a regolith of high amount of secondary minerals with a similar age is a clue for the identification of weathering pulses. In the present study, the four defined generations of kaolinite highlight the presence of at least four weathering events

since the Eocene. The age variation within each family does not exceed 3 Ma. This characterizes short weathering pulses that have affected the Karnataka plateau. In this section, possible relations between age groups and climatic and geomorphologic events that occurred in the Southern Peninsular India since 40 Ma (Zoom of the last 15 Ma in Fig. 12) are discussed. The previously given ages are also compared with the evolution of the global continental drainage curve made by Tardy and Roquin, 1998. As a rough approximation, global continental drainage peaks could correspond to most favorable periods of weathering.

The 39 Ma kaolinite age group (Table 3), observed in the Payoddu profile, is the oldest clue of past laterite development in the Karnataka plateau. This old age is very close to the transient Mid-Eocene Climatic Optimum (around 41 Ma), a temperature peak as defined from global oceanic temperature (Bohaty et al., 2009; Zachos et al., 2008). Concomitant continental and monsoon intensification has been observed in the North West of China by Bosboom et al. (2014). A recent modeling study (Tada et al., 2016) also relates the onset of the Tibetan Plateau uplift to a precipitation strengthening in India at this period. Both events may have induced a weathering pulse on the Karnataka plateau. It is also important to consider that at this period, a large part of India was located within the equatorial belt, with more intense precipitation than evaporation (Kent and Muttoni, 2008; Bonnet et al., 2016). The significant precipitation of the equatorial belt and the local annual mean temperature of 27 °C, estimated from Chatterjee et al. (2013), characterizing this part of India around this time period constituted favorable conditions for lateritic regolith development. The 39 Ma kaolinite group could thus result from regional south Indian climate variations due to the combination of local geodynamic factors and Mid-Eocene Climatic Optimum event.

Despite relatively high erosion rates (20 m·Ma^{-1} according to Mandal et al., 2015), old kaolinites can still be identified, which questions the constancy of erosion and the long term stability of the profile.

An important age gap is observed between 39 Ma and 9.83 Ma (the oldest sample of Mananthavady), attesting for the relictual nature of the oldest kaolinites. However, even if no weathering pulse was recorded within these profiles during this time range, several events could have influenced the local weathering conditions such as the weathering pulse observed in the Ghats around 28 Ma by Bonnet et al. (2016). In addition, a recent study (Retallack et al., 2018) also shows that paleosols at the edge of Himalaya have recorded the action of modern South Asiatic monsoon around 20 Ma. These observations could fit with the inception of the Asian monsoon described by Chatterjee et al. (2013) at 23 Ma despite the fact that this hypothesis is still disputed (Ramstein et al., 1997; Hubert and Goldner, 2012; Licht et al., 2014, 2015). However, this event is not recorded in any of the studied profiles, but this may have been erased by the recrystallization of younger kaolinite generations.

The 9 Ma group coincides with an important local weathering event which has been also observed in the Western Ghats region, in the lowland coastal plain, by Bonnet et al. (2016), but can hardly be correlated with a worldwide event because of the decline of the global continental drainage during this period of time (Fig. 12). This points to a more local cause. Zhisheng et al. (2001) and Chatterjee et al. (2013) described the onset of the modern Indian monsoon system about 9–8 Ma ago, in relation with an abrupt increase of the Tibetan Plateau elevation (Molnar et al., 1993, Zhisheng et al., 2001). Bonnet et al. (2016) correlated this local weathering event with this onset. However, as described above, our knowledge about the Indian monsoon onset has been recently updated by Retallack et al. (2018). Despite this fact, as both kaolinite and Mn oxide generations (Bonnet et al., 2016) are correlated, it must indicate the action of a weathering pulse during this period, that is probably linked to a strengthening of monsoonal precipitation induced by the 9–8 Ma Tibetan Plateau uplift. Several authors (e.g. Ramkumar et al., 2016) also explain that the Western Ghats Escarpment reached their present height around this period of time (i.e. 10–8 Ma), which may have driven significant climatic variations. Note that other authors,
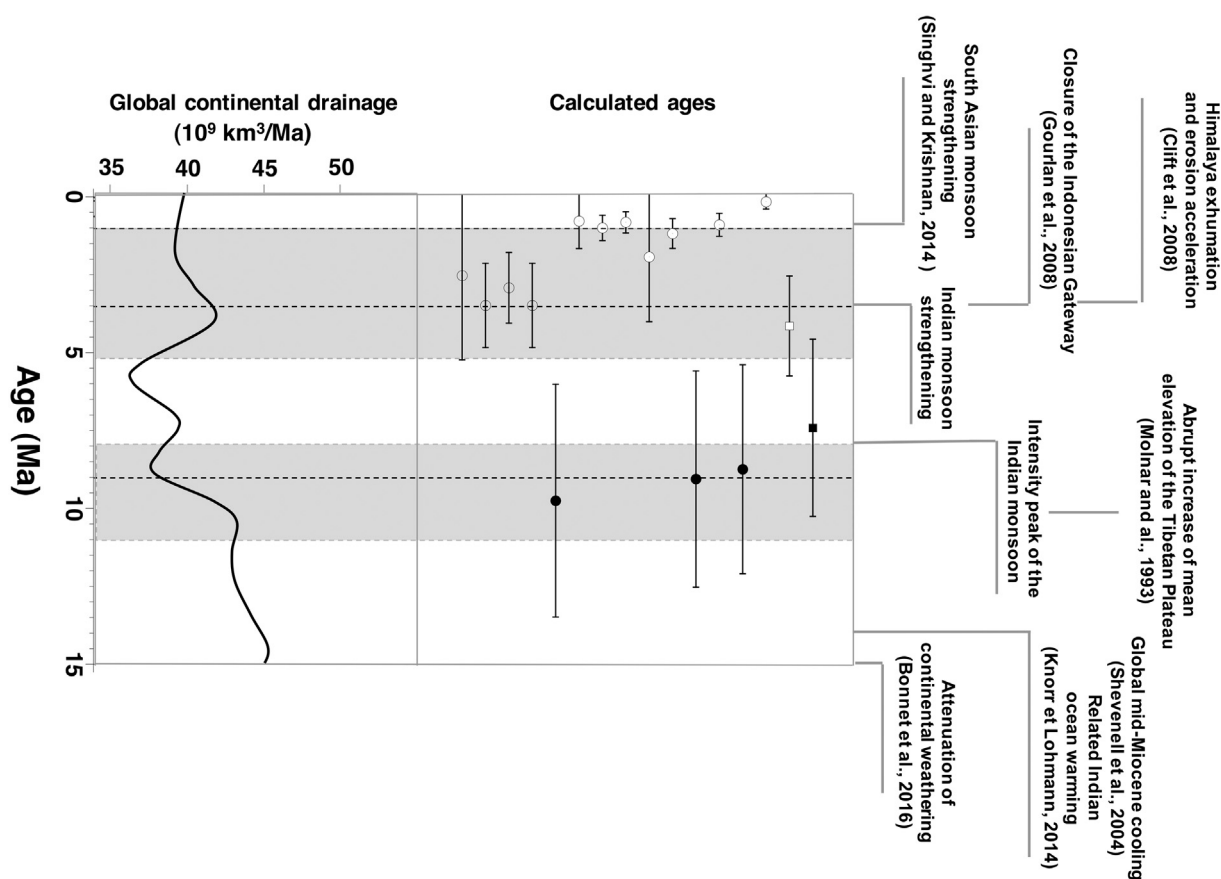
Fig. 12. Comparison between global continental drainage (from Tardy and Roquin, 1998) through the past 15 Ma and the age of the studied laterites. Major geodynamic and paleoclimatic regional events are listed as well as the weathering peak periods (in grey) described by Bonnet et al. (2016). The Mananthavady age families seems to be more correlated with the regional events that have affected the local climate than to the global climate and weathering evolution. The Payoddu samples are represented with squares and the Mananthavady ones with circles.

using weathering surface dating, explained that the WGE has been stabilized sooner in its history, in the early Eocene (Beauvais et al., 2016).

One of the recorded kaolinite age subgroup of the Mananthavady profile is set around 3.5 Ma. This group might be related to the acceleration of the Himalaya exhumation and erosion (Clift et al., 2008) and to the closure of the Indonesian Gateway (i.e. end of the Miocene Indian Ocean Equatorial Jet, Gourlan et al., 2008) where both the events took place around 3.5 Ma ago. The first event is currently linked to a monsoon strengthening, also observed by Zhisheng et al. (2001), which could have induced the formation of this kaolinite group. Bonnet et al. (2016) described a weathering pulse at 2.5 Ma that affected the secondary laterites of the coastal plains near to the Deccan plateau. Considering the EPR age uncertainties, these events, as well as the increase of the global continental drainage around this time period, could be related to the 3.5 Ma group of kaolinite from this study.

The 1 Ma kaolinites group (Fig. 12), only observed in Mananthavady, could be linked to the strengthening of the South Asian monsoon occurring between 1.44 and 0.34 Ma period, as inferred from the study of Chinese lake sediments (Singhvi and Krishnan, 2014, and ref. therein). Zhao et al. (2017) also noticed favorable conditions for kaolinite-rich laterite profile development between 1.2 and 1 Ma in southern China, which could confirm the existence of a south Asian weathering pulse at this time period. This could also be correlated with the rise of precipitation in southern India about 0.4 Ma ago, which is observed in the sediments and the pollens from the Southern Kerala Basin (Jayalakshmi et al., 2004). Despite the occurrence of global continental drainage (value around $39 \cdot 10^9$ km$^3 \cdot$ Ma^{-1}, according to Tardy and Roquin, 1992) during this period, close to the present days value, this 1 Ma age group could be, again, the result of local climatic forcing.

7. Conclusion

The present study addresses the dating complexity of old, tropical weathering covers that host several generations of the same secondary mineral. Most of the ages of the Mananthavady and Payoddu lateritic kaolinites are quite younger than the majority of the dated Mn-oxides of Deccan plateau lateritic duricrusts (Bonnet et al., 2016). Because of the kaolinite dissolution/recrystallization processes, only a minimal age estimate for these profiles can be given by the EPR dating: the Mananthavady profile is at least 9.83 Ma and the approximate age of Payoddu profile is at least 40.73 Ma.

The evolution of the studied regoliths from this study reveals short weathering pulses (around ca 3 Ma periods) rather than a continuous process of weathering as also noticed by other independent dating approaches implemented on different laterites (e.g. Vasconcelos et al., 1994; Retallack, 2010). Although, they cannot be interpreted as a proof of seasonality of rainfall, the identified weathering pulses are mostly correlated with the Asiatic monsoon evolution and strengthening. These pulses seem to be mainly caused by a subcontinental climatic forcing, rather than by global events.

This study shows the ability of EPR dating methodology to identify the main weathering periods that affected laterites. However, EPR dating has significant uncertainties compared to classical dating techniques, but no other dating technique can be applied so far on regolith where Mn oxides and well crystallized goethites are absent and ages are older than 1 Ma. In addition, this study showed a limiting test for the EPR dating methodology, with a set of concentrations around 1 ppm of U, 10 ppm of Th samples containing Fe oxides partly preserved from CBD attacks and recent kaolinite ages (0.2-1 Ma). Our data suggest

that it may be very difficult to date kaolinites below these combined values.

Thus, the EPR dating of phyllosilicates offers the possibility of removing the existing scientific barrier (Bourman, 1993) toward a detailed understanding of complex weathering processes and evolution of major continental surfaces.

Supplementary data to this article can be found online at https://doi.org/10.1016/j.gr.2018.12.003.

Acknowledgements

References

Adamiec, G., Aitken, M., 1998. Dose-rate conversion factors: update. Ancient TL 16 (2), 41–49.

Allard, T., Muller, J.P., 1998. Kaolinite as an in situ dosimeter for past radionuclide migration at the Earth's surface. Applied Geochemistry 13 (6), 751–765.

Allard, T., Muller, J.P., Dran, J.C., Ménager, M.T., 1994. Radiation-induced paramagnetic defects in natural kaolinites: alpha dosimetry with ion beam irradiation. Physics and Chemistry of Minerals 85–96.

Allard, T., Gautheron, C., Riffel, S.B., Balan, E., Soares, B.F., Pinna-Jamme, R., Derycke, A., Morin, G., Bueno, G.T., do Nascimento, N., 2018. Combined dating of goethites and kaolinites from ferruginous duricrusts. Deciphering the Late Neogene erosion history of Central Amazonia. Chemical Geology 479, 136–150.

Balan, E., Allard, T., Boizot, B., Morin, G., Muller, J.P., 1999. Structural Fe^{3+} in natural kaolinites: new insights from electron paramagnetic resonance spectra fitting at X and Q-band frequencies. Clays and Clay Minerals 47 (5), 605–616.

Balan, E., Allard, T., Boizot, B., Morin, G., Muller, J.P., 2000. Quantitative measurement of paramagnetic Fe^{3+} in kaolinite. Clays and Clay Minerals 48 (4), 439–445.

Balan, E., Fritsch, E., Allard, T., Calas, G., 2005. Formation and evolution of lateritic profiles in the middle Amazon basin: insights from radiation-induced defects in kaolinite. Geochimica et Cosmochimica Acta 69 (9), 2193–2204.

Balan, E., Fritsch, E., Allard, T., Calas, G., 2007. Inheritance vs. neoformation of kaolinite during lateritic soil formation: a case study in the middle Amazon Basin. Clays and Clay Minerals 55 (3), 253–259.

Beauvais, A., Ruffet, G., Hénocque, O., Colin, F., 2008. Chemical and physical erosion rhythms of the West African Cenozoic morphogenesis: The 39Ar-40Ar dating of supergene K-Mn oxides. J. Geophys. Res. Earth Surf. 113, F04007.

Beauvais, A., 2009. Ferricrete biochemical degradation on the rainforest-savannas boundary of Central African Republic. Geoderma 150, 379–388.

Beauvais, A., Bonnet, N.J., Chardon, D., Arnaud, N., Jayananda, M., 2016. Very long-term stability of passive margin escarpment constrained by $^{40}Ar/^{39}Ar$ dating of K-Mn oxides. Geology 44 (4), 299–302.

Benke, R.R., Kearfott, K.J., 2000. Accounting for ^{222}Rn loss during oven drying for the immediate laboratory gamma-ray spectroscopy of collected soil samples. Applied Radiation and Isotopes 52, 271–287.

Bird, M.I., Longstaffe, F.J., Fyfe, W.S., Kronberg, B.I., Kishida, A., 1993. An oxygen-isotope study of weathering in the Eastern Amazon basin, Brazil. Climate Change in Continental Isotopic Records. Geophysical Monograph 78, pp. 295–307.

Bohaty, S.M., Zachos, J.C., FLorindo, F., Delaney, M.L., 2009. Coupled greenhouse warming and deep-sea acidification in the Middle Eocene. Paleocenography 24 (2), PA2207.

Bonnet, N.J., Beauvais, A., Arnaud, N., Chardon, D., Jayananda, M., 2014. First $^{40}Ar/^{39}Ar$ dating of intense Late Palaeogene lateritic weathering in Peninsular India. Earth and Planetary Science Letters 386, 126–137.

Bonnet, N.J., Beauvais, A., Arnaud, N., Chardon, D., Jayananda, M., 2016. Cenozoic lateritic weathering and erosion history of Peninsular India from $^{40}Ar/^{39}Ar$ dating of supergene K-Mn oxides. Chemical Geology 446, 33–53.

Bosboom, R.E., Abels, H.A., Hoorn, C., Van den Berg, B.C.J., Gui, Z., Dupont-Nivet, G., 2014. Aridification in continental Asia after the Middle Eocene Climatic Optimum (MECO). Earth and Planetary Science Letters 389, 34–42.

Bourman, R.P., 1993. Perennial problems in the study of laterite: a review. Australian Journal of Earth Sciences 40, 387–401.

Brantley, S.L., Goldhaber, M.B., Ragnarsdottir, K.V., 2007. Crossing disciplines and scales to understand the critical zone. Elements 3, 307–314.

Brantley, S.L., 2010. Rock to regolith. Nat. Geosci. 3, 305–306.

Braun, J.J., Descloitres, M., Riotte, J., Fleury, S., Barbiéro, L., Boeglin, J.-L., Violette, A., Lacarce, E., Ruiz, L., Sekhar, M., Mohan Kumar, M.S., Subramanian, S., Dupré, B., 2009. Regolith mass balance inferred from combined mineralogical, geochemical and geophysical studies: Mule Hole gneissic watershed, South India. Geochimica et Cosmochimica Acta 73, 935–961.

Braun, J.J., Marechal, J.C., Riotte, J., Boeglin, J.L., Bedimo Bedimo, J.P., Ngoupayou, J.R.N., Nyeck, B., Robain, H., Sekhar, M., Audry, S., Viers, J., 2012. Elemental weathering fluxes and saprolite production rate in Central African lateritic terrain (Nsimi, South Cameroon). Geochimica et Cosmochimica Acta 99, 243–270.

Brimhall, G.H., Dietrich, W.E., 1987. Constitutive mass balance relations between chemical composition, volume, density, porosity and strain in metasomatic hydrochemical systems: results on weathering and pedogenesis. Geochimica et Cosmochimica Acta 51 (3), 567–587.

Brimhall, G.H., Lewis, C.J., Ford, C., Bratt, J., Taylor, G., Warin, O., 1991. Quantitative geochemical approach to pedogenesis: importance of parent material reduction, volumetric expansion and eolian influx in laterization. Geoderma 51, 51–91.

Chabaux, F., Ma, L., Stille, P., Pelt, E., Granet, M., Lemarchand, D., Di Chiara Roupert, R., Brantley, S.L., 2011. Determination of chemical weathering rates from U series nuclides in soils and weathering profiles: principles, applications and limitations. Applied Geochemistry 26, 20–23.

Chardon, D., Jayananda, M., Chetty, T.R., Peucat, J.J., 2008. Precambrian continental strain and shear zone patterns: South Indian case. Journal of Geophysical Research 113 (B8), 1–16.

Chatterjee, S., Goswami, A., Scotese, C.R., 2013. The longest voyage: tectonic, magmatic, and paleoclimatic evolution of the Indian plate during its northward fligt from Gondwana to Asia. Gondwana Research 23, 238–267.

Clift, P.D., Hodges, K.V., Heslop, D., Hannigan, R., Van Long, H., Calves, G., 2008. Correlation of Himalayan exhumation rates and Asian monsoon intensity. Nature Geoscience 875–880 (1 December 2008).

Clozel, B., Allard, T., Muller, J.P., 1994. Nature and stability of radiation-induced defects in natural kaolinites: new results and a reappraisal of published works. Clay and Clay Minerals 42 (6), 657–666.

Collier, J.S., Sansom, V., Ishizuka, O., Taylor, R., Minshull, T.A., Whitmarsh, R.B., 2008. Age of Seychelles-India break-up. Earth and Planetary Science Letters 272 (1–2), 264–277.

Dequincey, O., Chabaux, F., Clauer, N., Sigmarsson, O., Liewig, N., Leprun, J.C., 2002. Chemical mobilizations in laterites: evidence from trace elements and ^{238}U-^{223}U-^{230}Th disequilibria. Geochimica et Cosmochimica Acta 66 (7), 1197–1210.

Dixon, J.L., Von Blanckenburg, F., 2012. Soils as pacemakers and limiters of global silicate weathering. Comptes Rendus Geoscience 344 (11−12), 597–609.

Duval, M., 2012. Dose response curve of the ESR signal of the aluminium center in quartz grains extracted from sediment. Ancient TL 30, 41–49.

Farmer, V.C., 1974. The Layer Silicates: The Infrared Spectra of Minerals. 4. The Mineralogical Society, pp. 331–363.

Fritsch, E., Balan, E., Régina Do Nascimento, N., Allard, T., Bardy, M., Bueno, G., Derenne, S., Melfi, A.J., Calas, G., 2011. Deciphering the weathering processes using environmental mineralogy and geochemistry: towards an integrated model of laterite and podzol genesis in the Upper Amazon Basin. Comptes Rendus Geoscience 343, 188–198.

Gaite, J.M., Ermakoff, P., Allard, T., Muller, J.P., 1997. Paramagnetic Fe^{3+}: a sensitive probe for disorder in kaolinite. Clay and Clay Mineral 45, 496–505.

Girard, J.-P., Freyssinet, P., Chazot, G., 2000. Unraveling climatic changes from intraprofile variation in oxygen and hydrogen isotopic composition of goethite and kaolinite in laterites: an integrated study from Yaou, French Guiana. Geochimica et Cosmochimica Acta 64, 409–426.

Girard, J.-P., Freyssinet, P., Morillon, A.-C., 2002. Oxygen isotope study of Cayenne duricrust paleosurfaces: implications for past climate and laterization processes over French Guiana. Chemical Geology 191, 329–343.

Gourlan, A.T., Meynadier, L., Allègre, C.J., 2008. Tectonically driven changes in the Indian Ocean circulation over the last 25 Ma: neodymium isotope evidence. Earth and Planetary Science Letters 267, 353–364.

Guillocheau, F., Simon, B., Baby, G., Bessin, P., Robin, C., Dauteuil, O., 2018. Planation surfaces as a record of mantle dynamics: the case example of Africa. Gondwana Research 53, 82–98.

Gunnell, Y., 1997. Relief and Climate in South Asia: the influence of the Western Ghats on the current climate pattern of Peninsular India. International Journal of Climatology 17, 1169–1182.

Gunnell, Y., Bourgeon, G., 1997. Soil and climatic geomorphology on the Karnataka plateau, peninsular India. Catena 29, 239–262.

Gunnell, Y., Fleitout, L., 1998. Shoulder uplift of the Western Ghats passive margin, India: a denudational model. Earth Surface Processes and Landforms 23 (5), 391–404.

Gunnell, Y., Gallagher, K., Carter, A., Widdowson, M., Hurford, A.J., 2003. Denudation history of the continental margin of western peninsular India since the early Mesozoic-reconciling apatite fission-track data with geomorphology. Earth Planet. Sci. Lett. 215, 187–201.

Hubert, J., Goldner, A., 2012. Eocene monsoon. Journal of Asian Earth Sciences 44, 3–23.

Ikeya, M., 1993. New applications of electron spin resonance. Dating, Dosimetry and Microscopy. World Scientific Publishin Co. Pte. Ltd., Singapore.

Jayalakshmi, K., Nair, K.M., Kumai, H., Santosh, M., 2004. Late Pleistocene-Holocene Paleoclimatic history of the southern Kerala Basin, Southwest India. Gondwana Research 7 (2), 585–594.

Kale, V.S., Shejwalkar, N., 2008. Uplift along the western margin of the Deccan Basalt Province: is there any geomorphometric evidence? Journal of Earth System Science 117 (6), 959–971.

Kent, D.V., Muttoni, G., 2008. Equatorial convergence of India and early Cenozoic climate trends. PNAS 105 (42), 16065–16070. https://doi.org/10.1073/pnas.0805382105.

Kleeman, J.D., Lovering, J.F., 1967. Uranium distribution in rocks by fission-track registration in lexan plastic. Science 156 (3774), 512–513.

Kumar, A., 1986. Palaeolatitudes and the age of Indian laterites. Palaeogeography Palaeoclimatology Palaeoecology 53 (2–3), 231–237.

Langmuir, D., 1978. Uranium solution-mineral equilibria at low temperature with applications to sedimentary ore deposits. Geochimica et Cosmochimica Acta 42 (6A), 547–569.

Langmuir, D., Herman, J.S., 1980. The mobility of thorium in natural waters at low temperature. Geochimica et Cosmochimica Acta 44 (11), 1753–1766.

Licht, A., Van Capelle, M., Abels, H.A., Ladant, J.B., Trabuchi-Alexandre, J., France-Lanord, C., Donnadieu, Y., 2014. Asian monsoons in a late Eocene greenhouse world. Nature 513, 501–506.

Licht, A., Boura, A., De Fransceschi, D., Utescher, T., Sein, C., Jaeger, J.J., 2015. Late middle Eocene fossil wood of Myanmar: implications for the landscape and the climate of the Eocene Bengal Bay. Review of Palaeobotany and Palynology 216, 44–54.

Lucas, Y., 1989. Systèmes pedologiques en Amazonie brésilienne. Equilibres, déséquilibres et transformations. Université de Poitiers (Thèse N°211).

Lucas, Y., Chauvel, A., Ambrosi, J.P., 1986. Processes of aluminium and iron accumulation in latosols developed on quartz rich sediments from Central Amazonia (Manaus, Brazil). Geochemistry and Mineral Formation in the Earth Surface, pp. 289–299.

Lucas, Y., Nahon, D., Cornu, S., Eyrolle, F., 1996. Genèse et fonctionnement des sols en milieu équatorial. Comptes Rendus de l'Académie des Sciences 322, 1–16.

Mandal, S.K., Lupker, M., Burg, J.P., Valla, P.G., Haghipour, N., Christl, M., 2015. Spatial variability of ^{10}Be-derived erosion rates across the southern Peninsular Indian escarpment: a key to landscape evolution across passive margins. Earth and Planetary Science Letters 425, 154–167.

Mehra, O.P., Jackson, M.L., 1960. Iron oxide removal from soils and clays by a dithionite-citrate system buffered with sodium bicarbonate. Clays and Clay Minerals 7, 317–327.

Meunier, A., Caner, L., Hubert, F., El Albania, A., Prêt, D., 2013. The weathering intensity scale (WIS): an alternative approach of the chemical index of alteration (CIA). American Journal of Science 313, 113–143.

Molnar, P., England, P., Martinod, J., 1993. Mantle dynamics, uplift of the Tibetan Plateau, and the Indian monsoon. Reviews of Geophysics 31 (4), 357–396.

Muller, J.-P., Manceau, A., Calas, G., Allard, T., Ildefonse, Ph., Hazemann, J.-L., 1995. Crystal chemistry of kaolinite and Fe-Mn oxides: relation with formation conditions of low-temperature systems. American Journal of Science 295, 115–1155.

Nahon, D., 1991. Introduction to the petrology of soils and chemical weathering. A Wiley-Interscience Publication 97–134.

Nahon, D., 2003. Altérations dans la zone tropicale. Signification à travers les mécanismes anciens et/ou encore actuels. Comptes Rendus Geoscience 335, 1109–1119.

Nahon, D., Colin, F., 1982. Chemical weathering of orthopyroxenes under lateritic conditions. American Journal of Science 282, 1232–1243.

Nesbitt, H.W., Young, G.M., 1982. Early Proterozoic climates and plate motions inferred from major element chemistry of lutites. Nature 299, 715–717.

Oczkowski, H.L., Przegietka, K.R., Lankauf, K.R., Szmanda, J.B., 2000. Gamma spectrometry in thermoluminescence dating. Geochronometria 18, 57–62.

Oh, N.H., Richter, D.D., 2005. Elemental translocation and loss from three highly weathered soil-bedrock profiles in the southeastern United States. Geoderma 126, 5–25.

Price, P.B., Walker, R.M., 1963. Fossil tracks of charged particles in mica and the age of minerals. Journal of Geophysical Research 68 (16), 4847–4862.

Ramkumar, M., Menier, D., Mathew, M., Santosh, M., 2016. Geological, geophysical, and inherited tectonic imprints on the climate and contrasting coastal geomorphology of the Indian peninsula. Gondwana Research 36, 65–93.

Ramstein, G., Fluteau, F., Besse, J., Joussaume, S., 1997. Effect of orogeny, plate motion and land sea distribution on Eurasian climate change over the past 30 million years. Nature 386, 788–795.

Retallack, G.J., 2010. Lateritization and bauxitization events. Economic Geology 105, 655–667.

Retallack, G.J., Bajpai, S., Liu, X., Kapur, V.V., Pandey, S.K., 2018. Advent of strong Indian monsoon by 22 million years ago. Journal of Geology 126, 1–24.

Russel, J.D., Fraser, A.R., 1994. Infrared methods. Clay Mineralogy: Spectroscopic and Chemical Determinative Methods. Chapman et al., London, pp. 11–67.

Sakoda, A., Ishimori, Y., Yamaoka, K., 2011. A comprehensive review of radon emanation measurements for mineral, rock, soil, mail tailing and fly ash. Applied Radiation and Isotopes 69, 1422–1435.

Schmidt, P.W., Prasad, V., Ramam, P.K., 1983. Magnetic ages of some Indian laterites. Palaeogeography, Palaeoclimatology, Palaeoecology 44 (3–4), 185–202.

Selo, M., 1983. La fission nucléaire et sa signification en géochronomogie, paléothermométrie et géochimie. Applications à l'étude particulière des basaltes océaniques. Université Paris VI (Thèse d'état).

Singhvi, K.A., Krishnan, R., 2014. Past and the present climate of India. Landscape and Landforms of India, World Geomorphological Landscapes, pp. 15–23.

Tada, R., Zheng, H., Clift, P.D., 2016. Evolution and variability of the Asian monsoon and its potential linkage with uplift of the Himalaya and Tibetan Plateau. Prog. Earth Planet Sci., 3–4 https://doi.org/10.1186/s40645- 016-0080-y.

Tardy, Y., Roquin, C., 1998. Dérive des continents, paléoclimats et altérations tropicales. Editions BRGM, 11-47, 159-205, 217-229, 337-450. .

Tardy, Y., Kobilsek, B., Paquet, H., 1991. Mineralogical composition and geographical distribution of African and Brazilian periatlantic laterites. The influence of continental drift and tropical paleoclimate during the past 150 million years and implications for India and Australia. Journal of African Earth Sciences 12, 283–295.

Tardy, Y., 1993. Pétrologie des latérites et des sols tropicaux. pp. 401–404 Masson.

Vasconcelos, P.M., Renne, P.R., Brimhall, G.H., Becker, T.A., 1994. Direct dating of weathering phenomena by $^{40}Ar/^{39}Ar$ and K-Ar analysis of supergene K-Mn oxides. Geochimica et Cosmochimica Acta 6, 1635–1665.

Vasconcelos, P.M., 1999. K-Ar and 40Ar/39Ar geochronology of weathering processes. Annu. Rev. Earth Planet. Sci. 27 (1), 183–229.

Vasconcelos, P.M., Reich, M., Suster, D.L., 2015. The paleoclimatic signatures of supergene metal deposits. Elements 11, 317–322.

Violette, A., Goddéris, Y., Maréchal, J.-C., Riotte, J., Oliva, P., Kumar, M.S.M., Sekhar, M., Braun, J.-J., 2010. Modelling the chemical weathering fluxes at the watershed scale in the Tropics (Mule Hole, South India): relative contribution of the smectite/kaolinite assemblage versus primary minerals. Chemical Geology 277, 42–60.

West, A.J., Galy, A., Bickle, M., 2005. Tectonic and climatic controls on silicate weathering. Earth and Planetary Science Letters 235 (1–2), 299–304.

Widdowson, M., 1997. Tertiary palaeosurfaces of the SW Deccan, Western India: implications for passive margin uplift. Geological Society, London, Special Publications 120, 221–248.

Yapp, C.J., 2000. Climatic implications of surface domains in arrays of δD and $\delta^{18}O$ from hydroxyl minerals: goethite as an example. Geochimica et Cosmochimica Acta 64 (12), 2009–2025.

Zachos, J., Dickens, G.R., Zeebe, R.E., 2008. An early Cenozoic perspective on greenhouse warming and carbon-cycle dynamics. Nature 45 (17), 279–283.

Zhao, L., Hong, H., Fang, Q., Yin, K., Wang, C., Li, Z., Torrent, J., Cheng, F., Algeo, T.J., 2017. Monsoonal climate evolution in southern China since 1.2 Ma: New constraints from Fe-oxide records in red earth sediments from the Shengli section, Chendgu Basin. Palaeogeography, Palaeoclimatology, Palaeoecology 473, 1–15.

Zhisheng, A., Kutzbach, J.E., Prell, W.L., Porter, S.C., 2001. Evolution of Asian monsoons and phased uplift of the Himalaya-Tibetan Plateau since the Late Miocene times. Nature 411, 62–66.

Ziegler, J.F., Ziegler, M.D., Biersack, J.P., 2010. SRIM-The Stopping and Range of Ions in Matter.